

**Multiscale Mechanical Studies of Nacre from
Gastropod Mollusk *Trochus Niloticus***

by

Benjamin J.F. Bruet

Submitted to the Department of Materials Science and Engineering
in Partial Fulfillment of the Requirements for the Degree of


**Master of Science in Materials Science and Engineering
at the
Massachusetts Institute of Technology**

June 2004

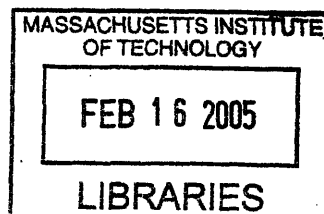
© 2004 Massachusetts of Technology
All rights reserved

Signature of Author.....

Department of Materials Science and Engineering
May 12, 2004

Certified by.....

Christine Ortiz
Associate Professor of Materials Science and Engineering
Thesis Supervisor

Accepted by.....
Carl V. Thompson II
Stavros Salapatas Professor of Materials Science and Engineering
Chairman, Departmental Committee on Graduate Students



Multiscale Mechanical Studies of Nacre from Gastropod Mollusk *Trochus Niloticus*

by

Benjamin J.F. Bruet

Submitted to the Department of Materials Science and Engineering
on May 12, 2004 in Partial Fulfillment of the Requirements for the Degree of
Master of Science in Materials Science and Engineering

Abstract

The inner columnar nacreous layer of the gastropod mollusk *Trochus Niloticus* is a nanostructured biocomposite with outstanding and unique mechanical properties. It is composed of ~95% wt of hexagonal aragonite plates (width= $5.8 \pm 0.4 \mu\text{m}$, thickness= $0.87 \pm 0.07 \mu\text{m}$), stacked ~40 nm apart, and ~5% wt of a biomacromolecular "glue" which exists between and within the individual plates. Atomic force microscopy (AFM) revealed a dense array of nanoasperities on the top and sides of the aragonite plates (~120 nm wide). A multiscale theoretical and experimental approach was taken to identify, understand, and predict the complex deformation mechanisms and mechanical behavior of this fascinating material.

Macroscopic 3-point bend tests yielded an in-plane Young modulus of $68.0 \pm 11.4 \text{ GPa}$ and $65.4 \pm 9.6 \text{ GPa}$ for freshly cut samples and samples soaked for 10 weeks respectively. A fracture strength of $231 \pm 34 \text{ MPa}$ and $213 \pm 42 \text{ MPa}$ respectively were measured. Samples soaked for 10 weeks, even if slightly less strong, exhibited major non-linearities in the stress-strain curves, emphasizing the greater toughness of hydrated nacre. Uniaxial compression yielded Young moduli of $63.8 \pm 14.7 \text{ GPa}$ for samples with the brick layers oriented parallel to the load, $19.1 \pm 3.4 \text{ GPa}$ when oriented perpendicular to it and fracture strengths of respectively 225 ± 44 and $663 \pm 71 \text{ MPa}$. The discrepancy between the compression moduli emphasizes that very distinct deformation mechanisms prevail during these tests, which is confirmed by the fact that fracture occurs also in three different ways (respectively through thickness, interlaminar and shatter). Scanning electron microscopy (SEM) and AFM of fractured samples revealed jagged and branched crack fronts at plate interface, tortuous crack paths, non-uniform angles of polygons (suggesting possible intrinsic deformability and displacement/sliding).

The technique of nanoindentation was carried out on individual aragonite tablets using a diamond-coated Berkovich probe tip (end-radius of 70 nm, tip angle of 142.3

degrees), at a rate of indentation of $10 \mu\text{N/s}$ (load controlled), forces from 10 to $1000 \mu\text{N}$ and indentation depths from 10 to 97 nm. AFM inspection of the indented region showed the existence of extensive plastic deformation within the tablet and suggested that occluded biomacromolecules may play a significant role in the deformation at loads below $100 \mu\text{N}$. Using the contact elastic theory, a Young modulus of 112.3 GPa and a hardness of 10.5 GPa were found for an individual platelet.

This study shows that a biocomposite principally composed of a poor ceramic (aragonite) can achieve surprisingly good macroscopic mechanical properties thanks to a complex hierarchical structure allowing an extraordinary variety of energy-dissipating mechanisms. Our aim is to continue to formulate multiscale structure-property relationships to eventually aid in the design and advancement of new synthetic biologically inspired lightweight, hard body armor technologies.

Thesis Supervisor: Christine Ortiz

Title: Associate Professor of Materials Science and Engineering

TABLE OF CONTENTS

ABSTRACT	3
TABLE OF CONTENTS	6
LIST OF ILLUSTRATIONS AND FIGURES	9
LIST OF TABLES	13
ACKNOWLEDGEMENTS	15
<hr/>	
INTRODUCTION	17
MODEL SYSTEM: NACRE FROM <i>T. NILOTICUS</i>	21
MATERIALS AND METHODS	25
Nacre	25
1. <i>Sample Preparation</i>	25
2. <i>Three-Point Bend Samples</i>	27
3. <i>Samples for Uniaxial Compression</i>	28
4. <i>Nanoindentation Samples</i>	30
5. <i>Atomic Force Microscopy (AFM) Samples</i>	30
6. <i>Scanning Electron Microscopy (SEM) Samples</i>	31
Calcite.....	31
Scanning Electron Microscopy	32

Atomic Force Microscopy	32
3-Point Bend Testing.....	34
Uniaxial Compression Testing	35
Nanoindentation	37
RESULTS	41
SEM Characterization	41
1. <i>Cross-section of 3-Point Bending Samples</i>	41
2. <i>Cleaved Compression Samples</i>	44
AFM Characterization.....	46
1. <i>Cross-section of 3-Point Bending Samples</i>	46
2. <i>Cleaved Compression Samples</i>	47
Three-point Bending Tests	50
Uniaxial Compression Tests.....	51
Observation of Fractured Regions after Macromechanical Testing.....	55
1. <i>Fractured Regions in 3-point Bending Samples</i>	55
2. <i>Fractured Region in Compression Samples</i>	56
Nanomechanical Testing	59
Observation of Indented Regions after Nanomechanical Testing.....	63
DISCUSSION	67
3-point Bend Tests.....	67
Compression Tests	68
Nanoindentation	69

CONCLUSION 74

APPENDIX 78

The Oliver-Pharr Analysis method..... 78

REFERENCES 82

LIST OF ILLUSTRATIONS AND FIGURES

All dimensions indicated in the title of figures correspond to the bottom border of the figure actual length.

Figure 1	Trochus Niloticus seashell.....	21
Figure 2	Nacreous (mother of pearl) columnar microstructure.....	22
Figure 3	Aragonite pseudo-hexagonal unit cell - from [22].....	22
Figure 4	Nacre formation mechanism – from [23].....	23
Figure 5	SEM of nanoasperities on a cross-section of abalone nacre tablets - from [3]	23
Figure 6	SEM of nanoasperities and organic matrix on abalone nacre tablets – from [3].....	23
Figure 7	<i>Trochus Niloticus</i> cross-section.....	26
Figure 8	3-point bending sample dimensions.....	27
Figure 9	Orientation of the nacreous layers for 3-point bending.....	28
Figure 10	Compression sample dimensions.....	28
Figure 11	Orientation of the layers for the 1 st group of compression samples.....	29
Figure 12	Orientation of the layers for the 2 nd group of compression samples.....	29
Figure 13	Uniaxial compression tests caused interlaminar failure.....	30
Figure 14	Cross-sectional failure of a 3-point bending sample.....	31
Figure 15	Mounting of the sample for 3-point bending.....	34

Figure 16	Schematic of the indentation of a nacre tablet.....	37
Figure 17	SEM images (60 μm) of the prismatic-nacreous columnar boundary.....	41
Figure 18	SEM image (120 μm): inner microlaminate columnar nacreous structure of T. Niloticus.....	42
Figure 19	SEM image (20 μm): Detail of the columnar structure.....	42
Figure 20	Distribution of the diameters of the nacreous platelets.....	43
Figure 21	SEM image (400 nm) of an interstice between two nacre platelets.....	43
Figure 22	SEM image (70 μm) of two superimposed nacreous layers of T. Niloticus..	44
Figure 23	SEM image (120 μm) of the top of a desiccated nacreous layer.....	45
Figure 24	SEM image (30 μm). Details of the desiccated bricks.....	45
Figure 25	SEM image (90 μm) of the top of a desiccated nacreous layer.....	46
Figure 26	SEM image (30 μm) of desiccated bricks with oriented striations.....	46
Figure 27	AFM image of the cross-section of the columnar nacreous layer.....	46
Figure 28	Distribution of the thickness of the nacreous platelets.....	47
Figure 29	AFM image (30 μm) of the surface of platelets.....	48
Figure 30	AFM image (10 μm) of the surface of a single brick.....	48
Figure 31	AFM image (30 μm) of nucleation site (center) of a platelet.....	48
Figure 32	Distribution of the diameters of the nanoasperities.....	49
Figure 33	AFM image (4 μm) of the partial edge of a brick shared by to stacked layers	50
Figure 34	AFM image (4 μm) of the edge of a brick lying on a nacreous layer.....	50
Figure 35	Averaged Load versus Deflection curves from 3-point bend testing of dry nacre.....	52

Figure 36	Averaged Load versus Deflection curves from 3-point bend testing of wet nacre.....	52
Figure 37	Averaged Stress versus Strain curves from compression testing of nacre with the layers parallel to the load.....	54
Figure 38	Averaged Stress versus Strain curves from compression testing of nacre with the layers perpendicular to the load.....	54
Figure 39	SEM image (300 μm) of the fracture surface of a broken 3-point bending sample.....	55
Figure 40	SEM image (350 μm) of columnar microstructure.....	57
Figure 41	SEM image (100 μm) of columnar microstructure.....	57
Figure 42	SEM image (300 μm scan) of a large through-thickness crack.....	57
Figure 43	SEM image (30 μm scan) of a small through-thickness crack.....	57
Figure 44	SEM image (50 μm scan) of in-plane branched microcracks.....	57
Figure 45	SEM image (15 μm scan). Detail of a microcrack.....	57
Figure 46	AFM image (30 μm scan) of fractured nacreous layers superimposed.....	58
Figure 47	AFM image (15 μm scan) of a cracked edge and microcrack running between platelets.....	58
Figure 48	Single Load vs. Indentation Depth curve during nanoindentation testing of dry nacre.....	60
Figure 49	Averaged Load (50 to 250) vs. Indentation Depth curves from nano-indentation testing of dry nacre, wet nacre and calcite.....	61
Figure 50	Averaged Load (500 to 1000) vs. Indentation Depth curves from nano-indentation testing of dry nacre, wet nacre and calcite.....	61
Figure 51	Averaged Young Modulus calculated from nanoindentation curves of dry nacre, wet nacre and calcite.....	62
Figure 52	Averaged Hardness calculated from nanoindentation curves of dry nacre, wet nacre and calcite.....	62

Figure 53 AFM image in air (2.5 μm scan): 9 mN indent mark on a platelet surface (dry nacre).....63

Figure 54 AFM image in air (3 μm scan): 5 mN indent mark on a platelet surface (wet nacre).....64

LIST OF TABLES

Table 1	<i>Trochus Niloticus</i> Taxonomy.....	21
Table 2	3-point bending properties of dry and wet nacre.....	51
Table 3	Compression properties of nacre relative to layer orientation.....	53
Table 4	Nanoindentation properties of dry nacre, wet nacre and calcite (1000 μ N max load).....	60

ACKNOWLEDGEMENTS

The almost two years of work necessary to gather the results presented in this thesis have been a challenging but very rewarding time in my life. I have learned much more than I thought I would ever about what research really is and how it should be conducted. When I first arrived here, I imagined I was entering the last step of my education before quickly starting working. I have now the feeling that I have met a new world of knowledge and that I am experiencing a new approach to science and engineering. All these reasons gave me the desire to move on a PhD and I am truly excited about spending the coming years at MIT.

I express my deepest gratitude to Professor Christine Ortiz for her invaluable guidance and advice as the research and thesis progress. Her enthusiastic supervising has contributed much to my well being at MIT.

I would like to thank Lauren E. Frick and Connie H. King for their contribution to this work as students participating in the Undergraduate Research Opportunity Program, Kuangshin Tai for his kind help on different experiments and the OPML group for its nice and friendly atmosphere. I gratefully acknowledge Mike Frongillo and the MIT-CMSE Electron Microscopy SEF, Alan Schwartzman and the MIT NanoLab, and finally the MIT Institute for Soldier Nanotechnologies for funding this project and for making wonderful labs available.

This sometimes intense period of my life would not have been so interesting and gratifying without my friends with whom my life has just been a deep, crazy and sincere enjoyment.

Most of all, I want to thank my parents, Aleth and Bernard, for the freedom, intelligence and love they have shown to me since I was born. They have given infinitely more than life to me.

INTRODUCTION

Through millions of years of evolution, nature has ingeniously created innumerate nanoscale structural design principles to produce multifunctional, lightweight materials with exceptional mechanical properties like seashell nacre, even though they are composed of relatively weak constituents available in the surrounding environment, e.g. bioceramics such as calcium carbonate and biomacromolecules such as proteins¹⁻⁸. Most natural materials exhibit a combination of outstanding fracture toughness, impact resistance, and stiffness due to their complex, hierarchical, multilayered nanocomposite structures which typically undergo a wide variety of poorly understood deformation mechanisms at many length scales. Some of these may include rupture of "sacrificial" weaker bonds, extension, pull-out, and/or ligament formation of a macromolecular component bridging an interface, void formation, bulk plastic deformation, crack blunting, pinning and branching, localized plastic deformation ahead of a crack tip, viscoelastic deformation, and interacting nanoasperities and mechanical interlocking. Many of these energy-dissipating mechanisms are barely, if at all, being exploited in currently used synthetic hard body armor systems.

The object of this thesis is to use a synergistic multiscale experimental and theoretical approach to study natural biocomposite materials in order to discover new and

more effective energy-dissipating deformation mechanisms and to understand their relationship to nanostructured design principles. The model system chosen to be studied is the inner columnar, microlaminate aragonite-based nacreous layer of the seashell *Trochus Niloticus* (gastropod mollusk). While nacreous layers from similar species have been shown to possess outstanding macroscopic mechanical properties¹⁻⁸, the molecular origins of this behavior, i.e. the ultrastructure, nanomechanical properties, and nanoscale deformation mechanisms are still largely unknown. A unique combination of standard macroscale mechanical testing methods, a variety of novel nanomechanical and ultrastructural imaging techniques and structural characterization are here used to provide an unprecedented fundamental understanding of the chosen model system. The overall objective will be achieved via three specific aims including:

- 1) to establish macroscopic mechanical properties, in particular energy-absorbing and fracture deformation mechanisms
- 2) to conduct nanomechanical studies to determine the molecular origins of macroscopic behavior
- 3) to assess the ability of multiscale, continuum finite element analysis (FEA) simulations to predict mechanical behavior
- 4) to understand how biochemical and structural characterization aspects determine nanomechanical properties.

In the longer term, the fundamental scientific laws established could be employed to aid in the design and advancement of new synthetic biologically inspired lightweight composite materials, hard body armor technologies; in particular helmets and protection

plates for specific body locations.

MODEL SYSTEM: NACRE FROM *T. NILOTICUS*

Trochus Niloticus (Fig. 1) is a gastropod mollusk (see Table 1) commonly found near the coasts of the Indian Ocean. Typically, the shells of gastropod mollusks are known⁶⁻⁹ to have many features in common, particularly concerning their microstructure.

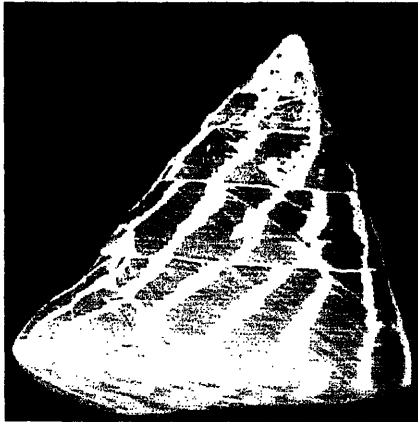


Fig. 1: *Trochus Niloticus* seashell

Phylum : Mollusca

Class : Gastropoda (snails, slugs)

Order : Archaeogastropoda

SuperFamily : Trochoidea

Family : Trochidae (Trochinae)

Genus : Trochus

Species : Niloticus

Common name : Pearl Trocha

Table 1: *Trochus Niloticus* Taxonomy

Several microscopic layers compose this shell, including (principal component in parenthesis):

- outermost: periostracum (thin organic layer composed mainly of sclerotized protein)

- prismatic (calcite)
- laminar columnar, nacreous (aragonite)
- innermost : irregular crossed-lamellar (calcite)

The tough inner microlaminate columnar nacreous layer (Fig. 2) is made of 95 wt% polygonal to rounded mostly aragonitic single crystal tablets in parallel sheets^{7,8}. Aragonite (Fig. 3) is a metastable form of CaCO₃. Coinciding centers determine the

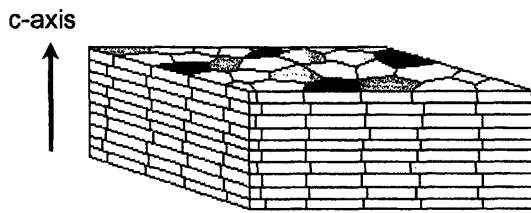


Fig. 2: Nacreous (mother of pearl) columnar microstructure

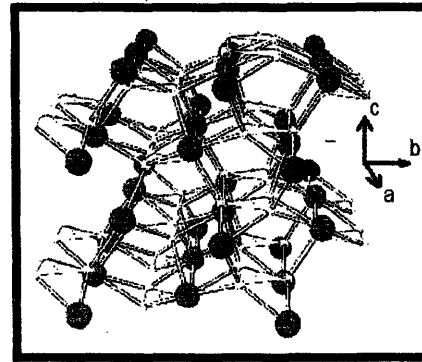


Fig. 3: Aragonite pseudo-hexagonal unit cell [22]

nucleation site of the overlying tablet⁷ and mineral is continuous through bulk via c-axis bridges¹⁰ (Fig. 4). The surface of the bricks is usually covered with nanoasperities (Fig. 5). The rest of the material is composed of biomacromolecules that represents up to 5 wt%¹¹. It is observable in the form of nm-thick layer between the aragonite plates¹² as well as within plates¹³.

The inner columnar nacreous layer has been shown to possess outstanding macroscopic mechanical properties. Toughness of nacre has been found to be 30 times greater than pure aragonite¹ while exhibiting an in-plane Young modulus of about 70 GPa^{1,3} Measurement of fracture toughness yield values⁴ of $7 \pm 3 \text{ MPa}^{1/2}$ while an average value of $180 \pm 120 \text{ MPa}$ has been determined for columnar laminated nacre⁴. Nacre

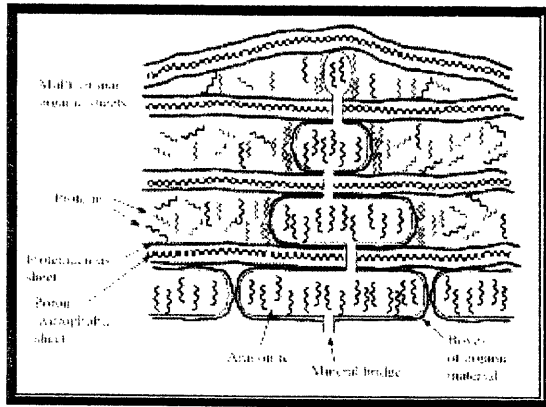


Fig. 4: Nacre formation mechanism [23]

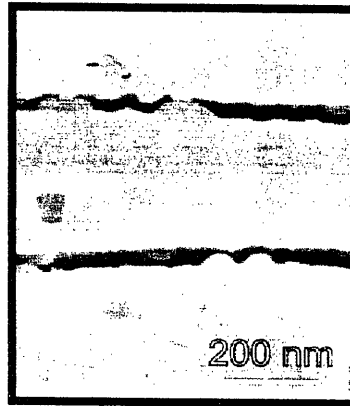


Fig. 5: SEM of nanoasperities on a cross-section of abalone nacre tablets [3]

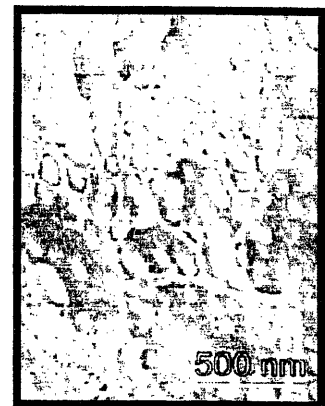


Fig. 6: SEM of nanoasperities and organic matrix on abalone nacre tablets [3]

having soaked in water for several weeks is known to show larger plasticity than dry nacre¹. Its work of fracture has been found to be 3000 times greater than pure aragonite¹ and many micromechanisms believed to dissipate efficiently the energy upon impact have been identified^{1,3,5}. However, the molecular origins of this behavior, i.e. the nanostructure, nanomechanical properties, and nanoscale deformation mechanisms are still largely unknown.

MATERIALS AND METHODS

Nacre

The *Trochus Niloticus* shell specimens (size about 10 cm) studied here were purchased from *Shell Horizons*, Clearwater FL. The nacre samples were obtained from the inner layers of the shell (columnar nacreous layers) according to the following preparation protocol.

1. Sample Preparation

The least destructive, minimum sample preparation procedure possible was employed including no alcohol dehydration, chemical fixation, or embedding. Samples were obtained from the flattest regions of the shell, as shown in Fig. 7. First, *Trocha Niloticus* shells were sectioned using a diamond impregnated annular wafering saw (*Buehler*, Isomet 5000) running at 800-900 rpm with constant “Isocut Plus”-based water solution irrigation. This solution was prepared by mixing 1/9 vol of concentrated *Buehler* “Isocut Plus” solution and 8/9 vol of water. The inner and outer layers, of other type than nacreous columnar, were removed during the designing of the samples. The samples of each series were cut from the same area of the same shell, to minimize variations due to

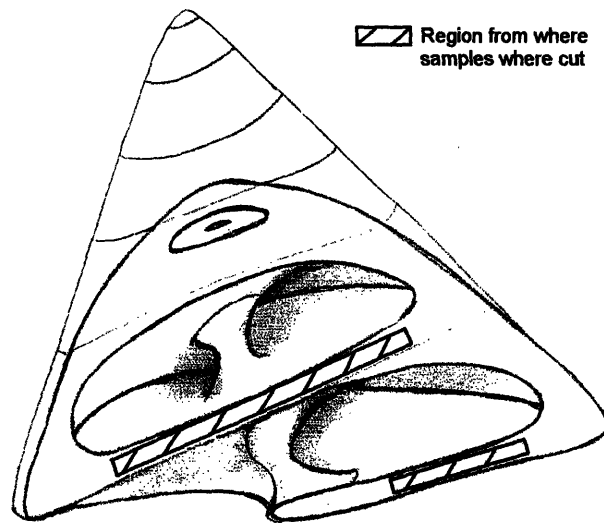


Fig.7: *Trochus Niloticus* cross-section

age, history of the shell, etc. Care was taken to obtain parallel sides, plane layers (by cutting where the curvature of the shell is minimal). The samples were then cleaned in distilled water for 30 minutes, using an Ultramet ultrasonic cleaner.

While the previous procedure was common for every sample further sample preparation was varied to produce three types of samples. The term “**dry sample**” refers to a sample tested immediately (within less than one hour) after completion of the previously described sample preparation procedure. The term “**wet sample**” refers to a sample that had been soaked for a certain number of weeks in artificial seawater¹⁴ (distilled water with 0.4221 mol/L NaCl, 0.011 mol/L KCl) in a hermetically sealed container at 20°C until use. Finally, the term “**dessicated samples**” refers to samples stored in an open container and that have been in contact with room air in 20°C for a certain number of weeks.

For 3-point bending and compression samples, every surface to be in contact with the

testing fixtures were polished down a metallographic polishing wheel (*Buehler*) (~100 rpm) and adhesive papers with successively smaller Al_2O_3 or SiO_2 particle grit sizes (*SBT, South Bay Technologies*) varied depending on the orientation of the layers, as described in detail in the following sections.

Before mechanical testing, all samples were individually measured using a micrometer, with a precision of $\sim 5 \mu\text{m}$. This was necessary to optimize the polishing times for the polished samples, and of course to plug the values in the stress-strain calculations. Following is the sample preparation protocol specific to each sort of test.

2. Three-Point Bend Samples

ASTM D5934 dimension requirements were not suitable due to the intrinsic thickness of the shell. Small samples were prepared according to the protocol reported in [3]. The samples were designed to be parallelepipedal, 12 mm in length, 2.5 mm in width and 0.5 mm in height (Fig. 8).

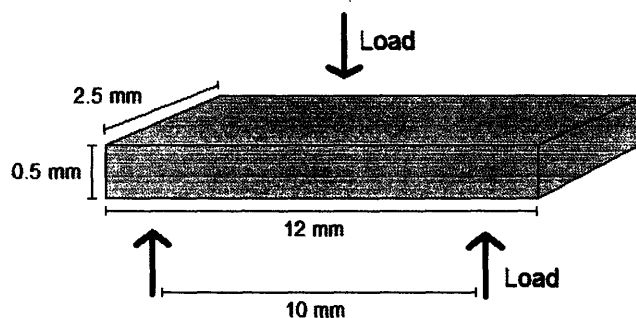


Fig. 8: 3-point bending sample dimensions

The samples had the lamellae boundaries parallel to the main surface (Fig. 9). They were polished (lubricant: water) on each main side ~ 1 min using a $1 \mu\text{m}$ Al_2O_3 disk then 3

min on a 0.05 μm Al_2O_3 disk at 1 lap/s. Polishing time was very short because the layers go off very easily with this orientation.

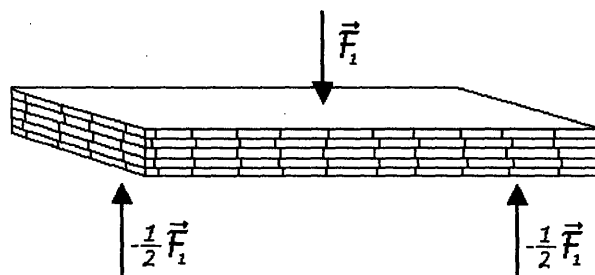


Fig. 9: Orientation of the nacreous layers for 3-point bending

3. Samples for Uniaxial Compression

ASTM D 695 dimension requirements were not suitable due to the intrinsic thickness of the shell. Small samples were prepared according to the protocol in [15]. Samples were designed to be parallelepipedal, with the following dimensions: length 2.5 mm, width 2.5

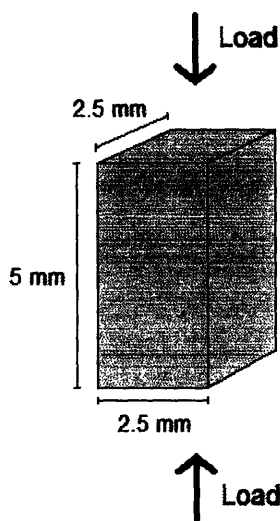


Fig. 10: Compression sample dimensions

mm and height 5 mm (Fig. 10).

The first group has the lamellae boundaries parallel to the main surface (Fig. 11). They were polished (lubricant: water) on each main side ~1 min using a 1 μm Al_2O_3 disk then 3 min on a 0.05 μm Al_2O_3 disk at 1 lap/s. Polishing time is very short because the layers go off very easily with this orientation.

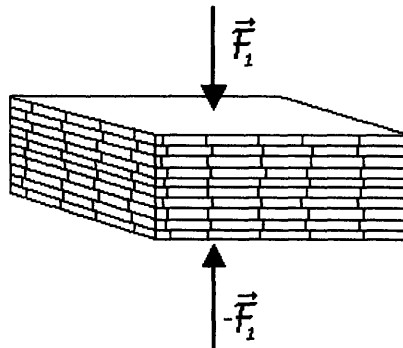


Fig. 11: Orientation of the layers for the 1st group of compression samples

The second group has the lamellae boundaries perpendicular to the main surface and parallel to the second biggest surface (Fig. 12). They were polished using SiO_2 disks up to 15 μm and then Al_2O_3 disks up to 0.05 μm (30 min on each main side).

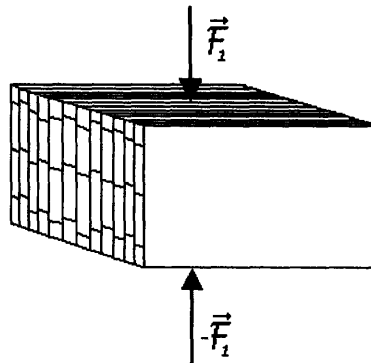


Fig. 12: Orientation of the layers for the 2nd group of compression samples

4. Nanoindentation Samples

Samples intended for nanoindentation testing were produced by cleavage of compression samples. The samples were obtained from uniaxial compression tests upon clean planar intertablet cleavage with minimal damage to the individual nacre tablets. These uniaxial compression tests have been carried out at 0.01 mm/min in ambient

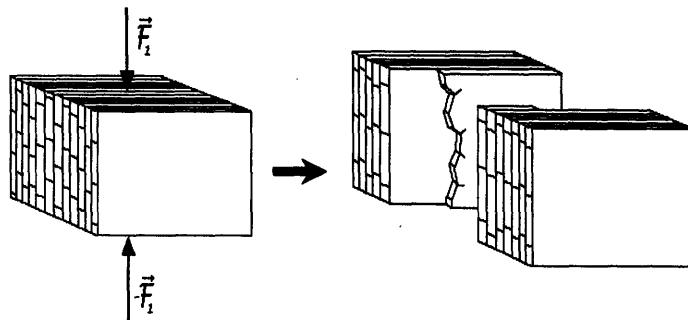


Fig. 13: Uniaxial compression tests caused interlaminar failure

conditions on freshly cut parallelepipedal samples (same dimensions as compression samples: 5 x 2.5 x 2.5mm) using a *Zwick* uniaxial tester (Model BTC-FR010TH.A50, with a 10 kN load cell). The applied load was parallel to nacre plate axis (Fig. 13), that is the aragonite c-axis (see previous chapter). The cleaved samples were then mounted on aluminum substrate plates using a minimum amount of Krazy Glue™, with the fractured/cleaved surface oriented upwards.

5. Atomic Force Microscopy (AFM) Samples

During this study, AFM imaging was carried out after 3 point-bending, compression and nanoindentation tests. Cleaved samples intended for AFM imaging were produced in

the same way as samples intended for nanoindentation. Such samples allowed the imaging of the top of bricks layers. The columnar nacreous structure could conveniently be studied by observing the cross-section of broken 3-point bending samples with the layer perpendicular to the force exerted (Fig. 14). In this case, fracture always takes place in the same plan as the probe, roughly in the middle of the span of the sample.

Mechanical samples (or pieces from them) were retrieved upon testing and mounted on aluminum substrate plates using a minimum amount of Crazy Glue, with the surface of interest oriented upwards.

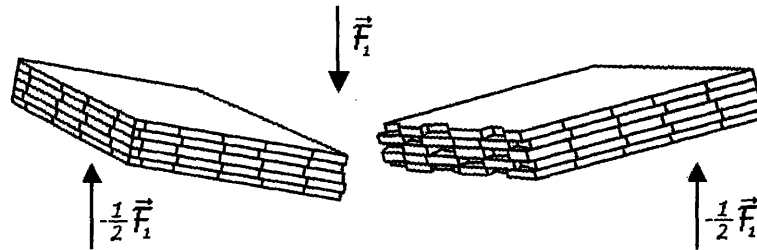


Fig. 14: Cross-sectional failure of a 3-point bending sample

6. Scanning Electron Microscopy (SEM) Samples

Samples intended for SEM imaging were produced in the same way as samples intended for AFM imaging. Before being inserted in the microscope chamber, samples for regular SEM were coated with Au-Pd 10 nm thick. Samples for Back Scattered Electron Microscopy (BSE) were inserted uncoated.

Calcite

Calcite pieces (size ~3 cm) were obtained from WARD'S Natural Science,

Rochester, NY. Only nanoindentation tests were carried on calcite. The sample preparation protocol followed was similar to the nanoindentation sample protocol for nacre.

Scanning Electron Microscopy

Unless specified otherwise, samples were coated with Au-Pd 10 nm thick, and imaged using a *JEOL SEM 6060*. The working distance was 6-9 mm, the sample plane was oriented perpendicular to the electron beam incidence. A 10-11 kV accelerating voltage was employed for dry samples and 19 kV for desiccated samples (less conductive).

Magnification greater than 100,000 times required the use of a *JEOL FV 6320*. In this case, samples were also coated with Au-Pd 10 nm thick. The working distance was 6 mm and the sample plane was oriented perpendicular to the electron beam incidence. A 5 kV accelerating voltage was employed.

Atomic Force Microscopy

Contact mode AFM imaging in ambient temperature and humidity was employed to produce surface topographical images of freshly cleaved samples. A *Digital Instruments* (DI, Santa Barbara, CA) Multimode SPM IIIA was used with an AS-130 "JV" piezoelectric scanner (X-Y scan range $\sim 125 \mu\text{m}$, vertical limit $\sim 5 \mu\text{m}$) and Veeco Standard Silicon Nitride Probes cantilevers (V-shaped with square pyramidal probe tip

geometry, tip half angles of $\sim 35^\circ$ cantilever length $\sim 200 \mu\text{m}$, nominal spring constant, $k \sim 0.32 \text{ N/m}$, and nominal probe tip radius of curvature $\sim 40 \text{ nm}$). A scan rate of 2 Hz using a maximum sample size of 512 x 512 pixels was set up. The drive amplitude and amplitude set-point were maximized to get the fullest peak upon tuning. Gains were chosen to maximize either the deflection image (gains ~ 1.0). The x- and y- scan directions were calibrated with a $10 \times 10 \mu\text{m}^2$ grid. The z direction was calibrated with 5 nm diameter beads on a cleaved mica surface. The scans were tested for typical AFM imaging artifacts by varying scan direction, scan size, and rotating the sample.

For nanoindentation samples in-situ imaging, a *Quesant* Q-Scope 350 was used with a PZT tube scanning element (X-Y scan range $\sim 40 \mu\text{m}$, vertical limit $\sim 4.5 \mu\text{m}$) and Si_3N_4 *Wavemode* NSC16 cantilevers (rectangular shaped with conical probe tip geometry, length $\sim 230 \mu\text{m}$, width $\sim 40 \mu\text{m}$, cone angle $< 20^\circ$, probe tip height $\sim 15\text{-}20 \mu\text{m}$, $f \sim 170 \text{ kHz}$, $k \sim 40 \text{ N/m}$, $R_{\text{TIP}} \sim 10 \text{ nm}$). The Q-scope was calibrated in the x- and y- scan directions with a calibration grating with lines spaced $1.0 \mu\text{m}$ apart. Z-direction calibration was done with a 10% sloped surface provided by the manufacturer. A scan rate of 2 Hz using a maximum sample size of 500 x 500 pixels was set up. The drive amplitude and amplitude set-point ($\sim 0.25 \text{ V}$) were maximized to get the fullest peak upon tuning. Gains were chosen to maximize either the deflection image (gains ~ 350). Again, the scans were tested for typical AFM imaging artifacts by varying scan direction, scan size, and rotating the sample.

3-Point Bend Testing

3-point bend tests were performed in ambient conditions using a Stable Micro System TA-Xtplus Texture Analyzer. The span of the support was 8 mm and the orientation of the layers as shown on Fig. 15.

Load controlled bending of the sample was performed by means of a standard Aluminum 3-point bending fixture. The radius curvature of the probe and the support was measured to be 1.55 mm. During the test, the probe was pushing downward on the middle of the sample at a speed of 0.01 mm/s. Every test was carried on until fracture of the sample.

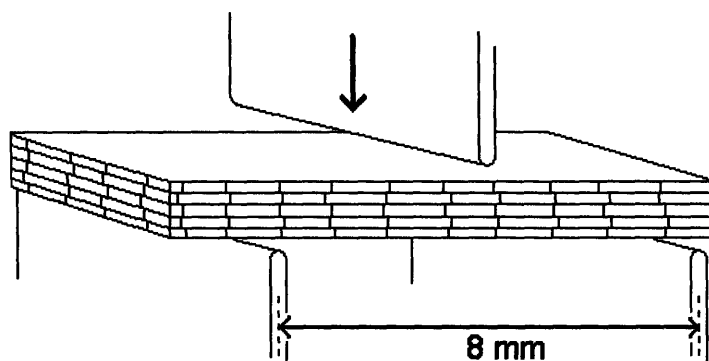


Fig. 15: Mounting of the sample for 3-point bending

25 dry and 8 wet samples were tested to obtain a statistically relevant dataset. The frame compliance was calibrated prior to each set of experiments and subtracted from the data measured according the following formula:

$$\frac{1}{\left(\frac{dF}{dD}\right)_{Sample}} = \frac{1}{\left(\frac{dF}{dD}\right)_{Measure}} - \frac{1}{\left(\frac{dF}{dD}\right)_{Machine}}$$

where F and D are the force (in N) exerted in the middle of the sample and its vertical deflection (in m) respectively. $\frac{1}{\left(\frac{dF}{dD}\right)_{Sample}}$ was found equal to 107.93 N/mm in average.

The 3-point bending Young modulus, fracture strength and maximal strain were calculated according to the following formulas (ASTM D-5934):

$$\varepsilon_f = \frac{6D_{\max}d}{L^2}$$

$$\sigma_f = \frac{3F_{\max}L}{2bd^2}$$

$$E = \frac{L^3}{4d^3b} \left(\frac{dF}{dD_{Sample}} \right)_{initial}$$

where :

- ε_f is the lateral strain before fracture,
- D_{\max} is the deflection before fracture (in m),
- d is the height of the sample (in m),
- L is the length of the sample (in m),
- b is the width of the sample (in m),
- σ_f is the Fracture Strength (in Pa),
- F is the force exerted on the sample (in N),
- E is the Young Modulus in tension (in Pa).

Uniaxial Compression Testing

Uniaxial compression tests were performed in ambient conditions using a Zwick uniaxial tester (Model BTC-FR010TH.A50, with a 10 kN load cell). Two orientations of

dry samples were tested, i.e. load parallel to nacre plate axis and load perpendicular to nacre plate axis. Load controlled compression of the sample was performed by means of a standard hardened steel compression plates. During the test, the probe was pushing downward on the middle of the sample at a speed of 0.01 mm/s until breakage. Every test was carried on until fracture of the sample.

18 samples were tested for each orientation in order to obtain a statistically relevant dataset. The frame compliance was calibrated prior to each set of experiments and removed from the data measured according the same formula as in the previous

section. $\frac{1}{\left(\frac{dF}{dD}\right)_{Sample}}$ was found equal to 179 kN/mm in average.

The compressive Young modulus, fracture strength and maximal strain were calculated according to the following formulas (ASTM D 695):

$$\varepsilon_f = \frac{h_{final}}{h_o}$$

$$\sigma_f = \frac{F_{final}}{A_o}$$

$$E = \frac{h_o}{A_o} \left(\frac{dF}{dh} \right)_{initial}$$

where:

ε_f is the lateral strain before fracture,

h is the height of the sample (in m),

A_0 is the initial top surface area (in m^2),

σ_f is the Fracture Strength (in Pa),

F is the force exerted on the sample (in N),

E is the Young Modulus in tension (in Pa).

Nanoindentation

Nanoindentation experiments (see Fig. 16) were conducted in ambient conditions using a *Hysitron, Inc.* (Minneapolis, MN) Triboindenter equipped with an AFM (*Quesant Q-Scope*) for tapping mode topographic imaging of residual impressions (see previous sections). Indentations were carried perpendicular to surface plane of platelet layers. The instrument is housed in a granite frame environmental isolation chamber so as to minimize instabilities due to the ambient background noise, active piezoelectric vibration control stages (Hysitron), and a thermal drift calibration step. Load-controlled nanoindentation was performed using a Berkovich (trigonal pyramid) diamond probe tip.

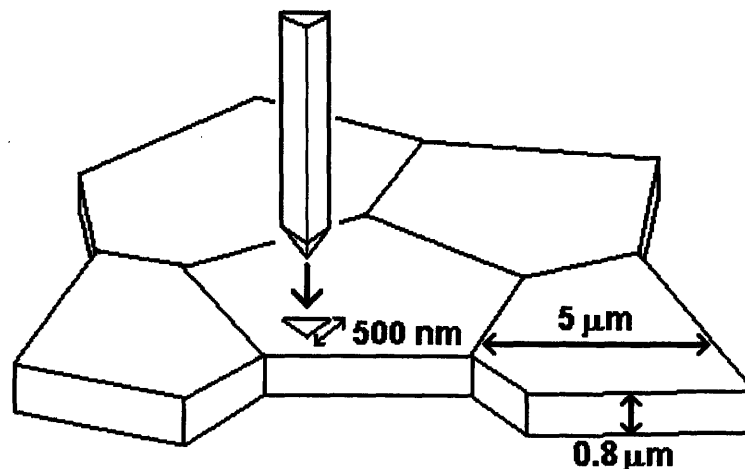


Fig. 16: Schematic of the indentation of a nacre tablet

The ideal geometry of a Berkovich probe tip is as follows; inclined face angle, $\alpha = 24.7^\circ$, apex angle, $\beta = 77.1^\circ$, projected contact area, $A_{\text{projected}} = 24.5h^2$ where h is the indentation depth, ratio of the projected to the surface area $A_{\text{projected}}/A_{\text{surface}} = 0.91$, ratio side length to indentation depth, $s/h = 7.5$, included half angle of the equivalent cone $\alpha = 70.3^\circ$, and projected edge length $a = 2h/\tan\alpha$. The force transducer is composed of three capacitor plates which impart force electrostatically, while concurrently measuring the displacement via the change in capacitance.

The transducer piezo was allowed to equilibrate for 660 seconds (60 last seconds with digital feedback) before each indent. The area function (see appendix) and the machine compliance were measured before every set of indents. The drift rate of the transducer was then automatically monitored by the software before indenting was initiated. The applied load function was divided into five segments as follows. The first segment consisted of a 3 second hold at zero force in which the probe tip is barely kept in contact with the sample, allowing for tip-sample equilibration. Segment two was a constant loading rate of $10 \mu\text{N}/\text{sec}$ and once the maximum set peak load was reached, the third segment, which was a hold period of 10 seconds, would ensue, to minimize creep effects. The fourth segment decrease the load until zero force with a constant unloading rate the same magnitude as that of segment two. The fifth segment would conclude the experiment with a 50 seconds hold at zero force, in order to calculate the final drift rate of the piezo. Maximum loads of 50, 100, 250, 500, 750 and $1000 \mu\text{N}$ were selected.

16 experiments per max load were performed in a square grid arrangement with each indent spaced $15 \mu\text{m}$ apart in order to obtain a statistically relevant dataset.

Locations on the sample were chosen randomly in the flattest area by means of the optical microscope attached to the nanoindenter. Load versus indentation distance curves from multiple experiments using the same maximum load and from different sample locations were averaged and standard deviations calculated and presented on the plots. The tip area function and frame compliance, were calibrated prior to each set of experiments using a fused quartz sample. Values for elastic modulus were calculated from the recommended 95% to 20% of the initial unloading curve by fitting these data to contact mechanical theory for an isotropic, elastic half-space (Oliver-Pharr or O-P method¹⁶, see Appendix) using n=400 number of individual curves. This geometric tip calibration was employed for all of the O-P fits to the experimental data to approximate the elastic moduli.

RESULTS

SEM Characterization

1. Cross-section of 3-Point Bending Samples

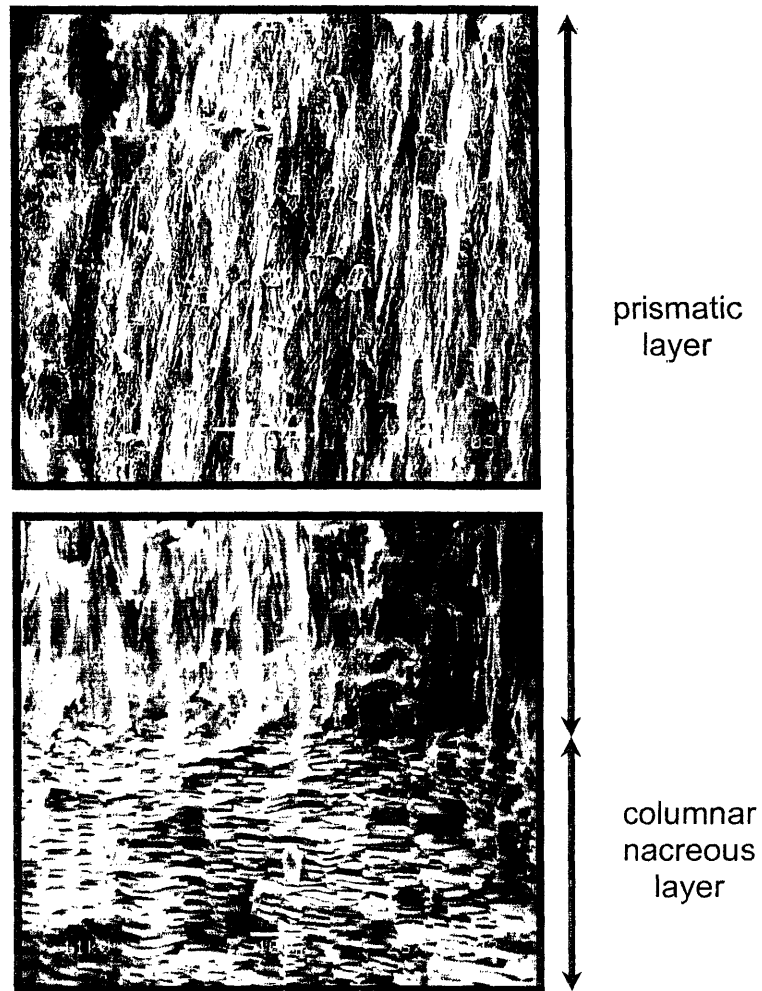


Fig. 17: SEM images (60 μm) of the prismatic - nacreous columnar boundary

Samples fractured in 3-point bending were imaged along their cross-section (see sample preparation section). The fractured surface imaged was thus parallel to the nacreous columns axis.

Different types of microscopic layers within *T. Niloticus* shell were observed (Fig. 17). The nacreous columnar layer is present in the core of the shell, usually spanning over a thickness of 2 mm. Other layer types are thinner and span over the inner and outer first millimeter of the shell. As visible in Fig. 17, the transition between the columnar nacreous layer and the adjacent layer is abrupt.



Fig. 18: SEM image (120 μm): inner microlaminate columnar nacreous structure of *T. Niloticus*

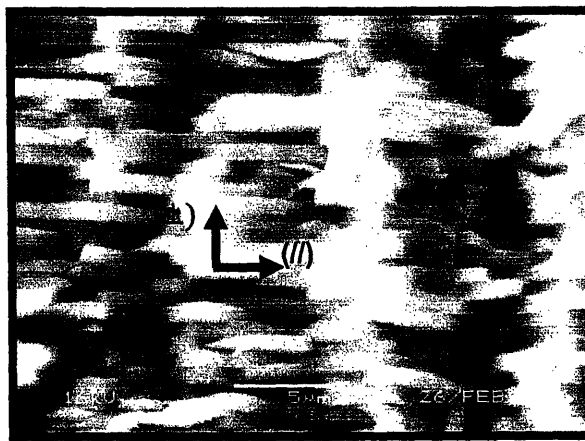


Fig. 19: SEM image (20 μm): Detail of the columnar structure

On Fig. 18, the nacreous columnar structure appears regular, each column being almost perfectly parallel to its neighbors. The zoom on Fig. 19 allows to notice not only the 1-D vertical order, but also the 2-D order in the plane perpendicular to the columns axis. Each nacre tablet is thus in the same plane as its neighbors from the adjacent columns. It is nevertheless observable that if the height and the center position of the bricks from a same stack varies only within a few percent, the shape of their outlines

exhibits a greater diversity. The sharpest edges are likely to be broken nacre tablets, as suggested by the presence of residual pieces.

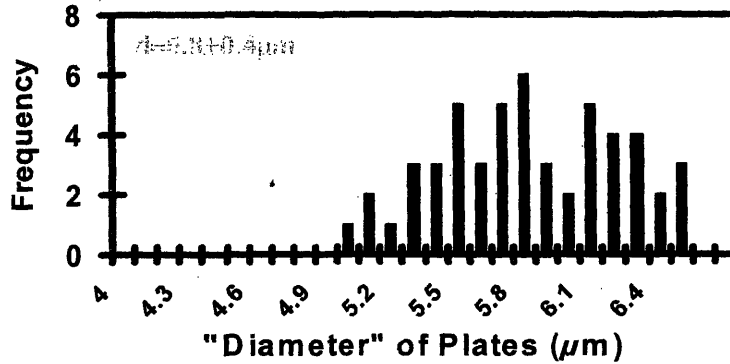


Fig. 20: Distribution of the diameters of the nacreous platelets

Averaging over 60 platelets yielded a mean width of $5.8 \pm 0.4 \mu\text{m}$ (Fig. 20). Thickness of the platelets was calculated on the basis of AFM images (see next section).

The observation of the matrix (filaments) requires a higher magnification, which could be achieved thanks to a *JEOL FV 6320*. Fig. 21 shows the space (about 50 nm) between two nacre platelets that have been pulled apart during 3-point bend testing. The



Fig. 21: SEM image (400 nm) of an interstice between two nacre platelets

matrix coating, which is normally less than 40 nm thick, is here observable in the form of proteins filaments linking the two aragonitic sides.

2. Cleaved Compression Samples

Samples cleaved by compression testing were imaged along the cleaved inner surfaces. The images taken this way show the top of the platelet layers (see sample preparation section). Fig. 22 was taken immediately after the sample was tested and required the contrast to be set a very high value in order to distinguish the relief of the surface. The layers appear continuous in-plane from plate to plate. Since the organic matrix covers entirely the platelets and smoothes their appearance, this image allows us

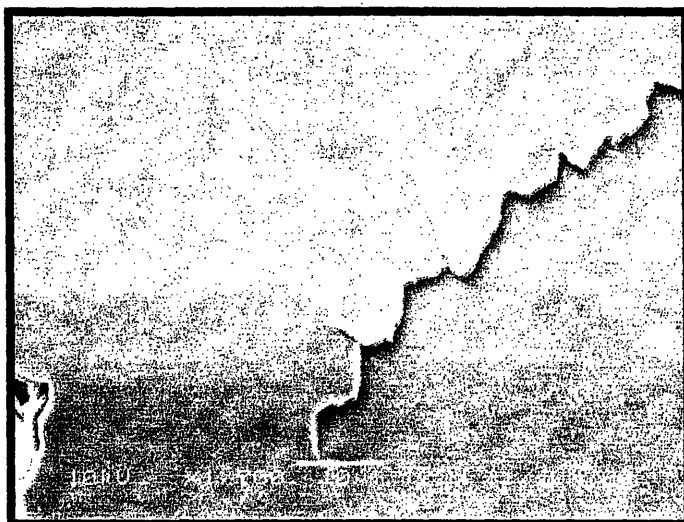


Fig. 22: SEM image (70 μm) of two superimposed nacreous layers of *T. Niloticus* to assess the evenness of the nacreous layers but makes the observation of platelet boundaries and nucleation centers difficult.

By letting a sample prepared in the same fashion dry out for a 10 weeks, we noticed that some elements of the structure dissolved in air. As shown on Fig. 23, the evaporated “mortar” (i.e. the organic matrix) has left an empty space inbetween the

bricks, as well as along radii drawn from the nucleation site of the bricks. This correlates with previous observations^{4,7} of embedded organic layers within the platelets. Each platelet seems to be the juxtaposition of aragonite monocrystalline sectors separated by thin organic walls that all converge toward the nucleation site.

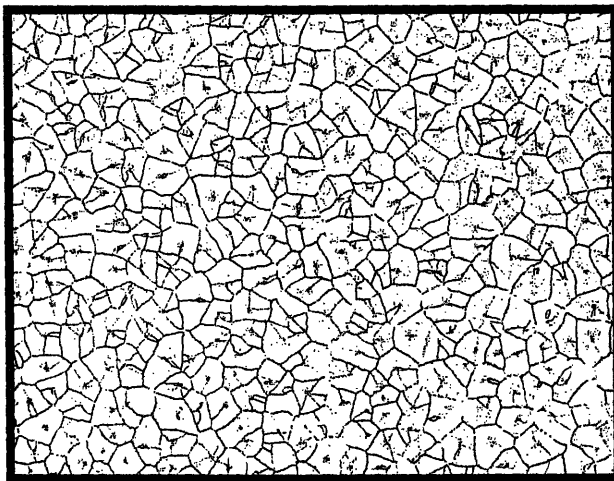


Fig. 23: SEM image (120 μm) of the top of a desiccated nacreous layer

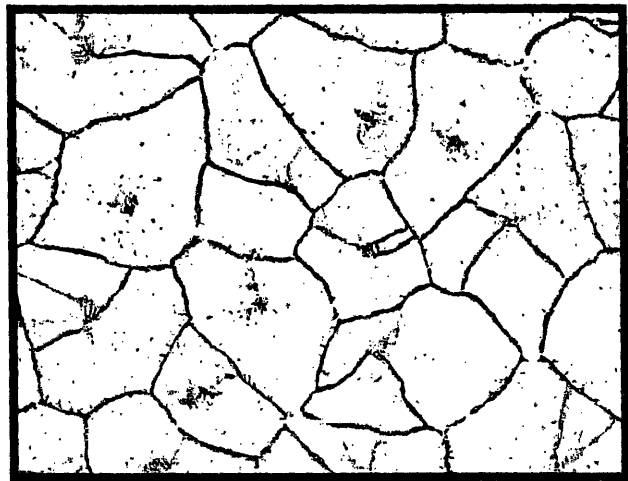


Fig. 24: SEM image (30 μm). Details of the desiccated bricks

This “pie” configuration is well illustrated by Fig. 24, which suggests that biomacromolecules within a brick are concentrated along walls but also on the nucleation site, which has been here replaced by a hole about 1 nm in diameter.

Interestingly, this dissolution phenomenon does not have a homogeneous appearance, as some regions of a same sample exhibit less deterioration, while others display larger damage to the aragonite parts of the bricks (Fig. 25). As it has been observed before^{4,7}, we can distinguish on Fig. 26 that the aragonite sectors within a brick have different crystalline orientation, which can be seen by the orientation of the striations in the calcified regions. Furthermore, each neighbor crystal appears twinned relative to its neighbors.

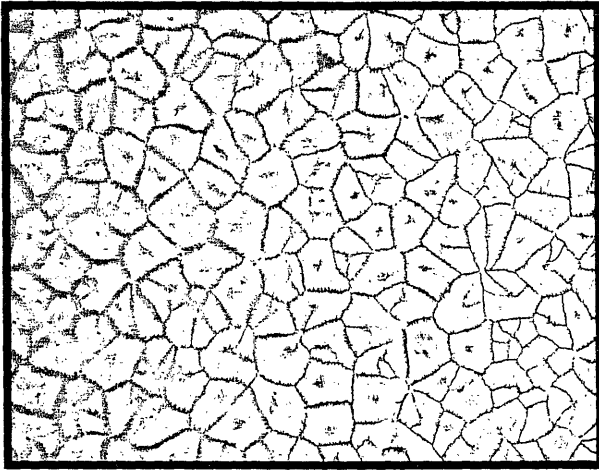


Fig. 25: SEM image (90 μm) of the top of a desiccated nacreous layer



Fig. 26: SEM image (30 μm) of desiccated bricks with oriented striations

AFM Characterization

1. Cross-section of 3-Point Bending Samples

The surface of broken 3-point bending samples exhibits a high roughness due to the irregular outlines of stacked platelets (see previous section). Sudden rises and drops make imaging very difficult. Some features of interest are nevertheless distinguishable

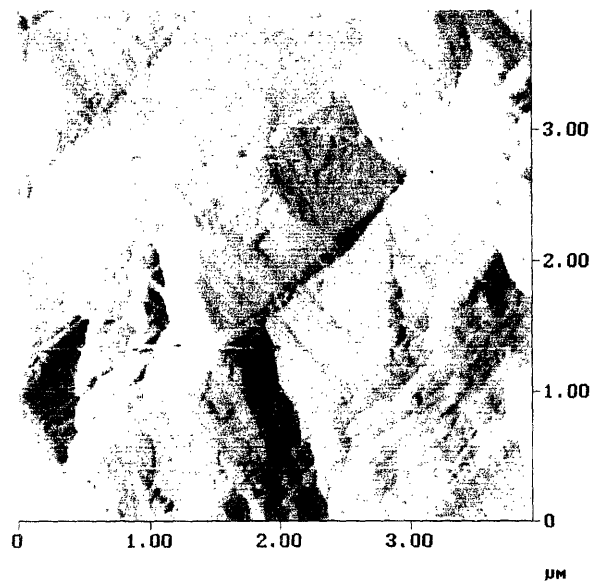


Fig. 27: AFM image of the cross-section of the columnar nacreous layer

thanks to the high resolution of AFM. Fig. 27 gives a good indication of the low variation of thickness amongst the bricks. The edges of the bricks appear quite differently whether they are cleaved or broken. Cleavage is indicated by the presence of a granular layer of biomacromolecules covering the surface. Breakage yield to a more regular surface but with a few sharp features corresponding to crack deflection. Averaging over 31 platelets yielded a mean thickness of $0.87 \pm 0.07 \mu\text{m}$ for the platelets (Fig. 28).

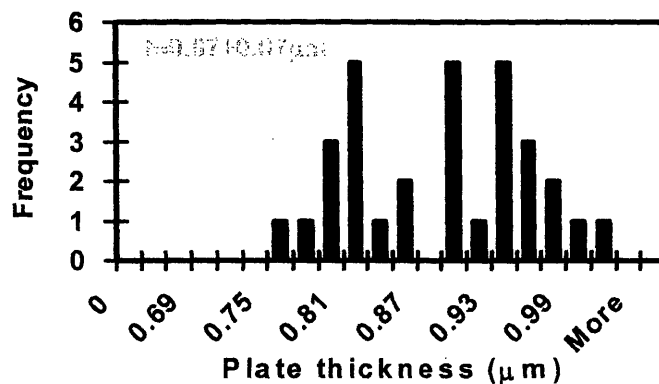


Fig. 28: Distribution of the thickness of the nacreous platelets

2. Cleaved Compression Samples

The clean cleavage resulting from compression tests of nacre samples produced surfaces of choice for AFM imaging. One of the great advantages of AFM compared to SEM is the possibility to quantitatively measure the height of things, and not only their length. The study of the surface of platelet layers shows that the maximal amplitude between high and low points is less than a hundred nanometers. As visible on Fig. 29, the highest features of the relief are localized on the boundaries of the bricks, in the form of grooves or slopes, and around a raised topographical feature in the center of

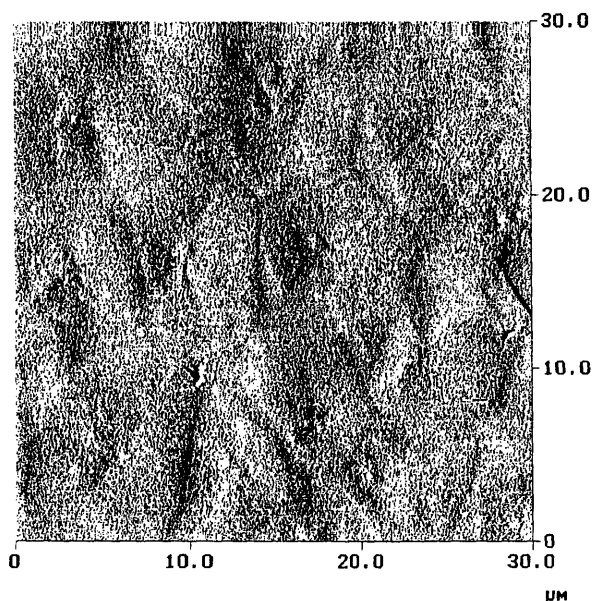


Fig. 29: AFM image (30 μm) of the surface of platelets

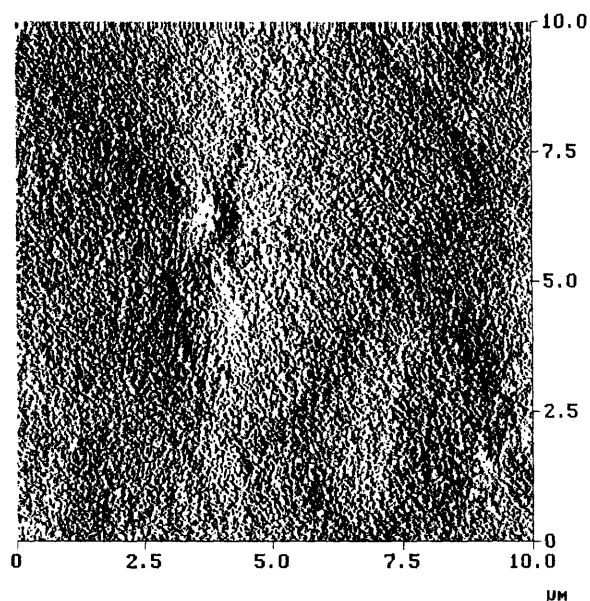


Fig. 30: AFM image (10 μm) of the surface of a single brick

biomineralization nucleation site. The latter appears to be a ~500 nm large and ~40 nm high bump and seems composed of a 20-30 overlapping nanoasperities (Fig. 30 and 31). On Fig. 29, the outlines of the approximately triangular sectors within the bricks also contribute to the overall roughness. We can also notice that defect holes are

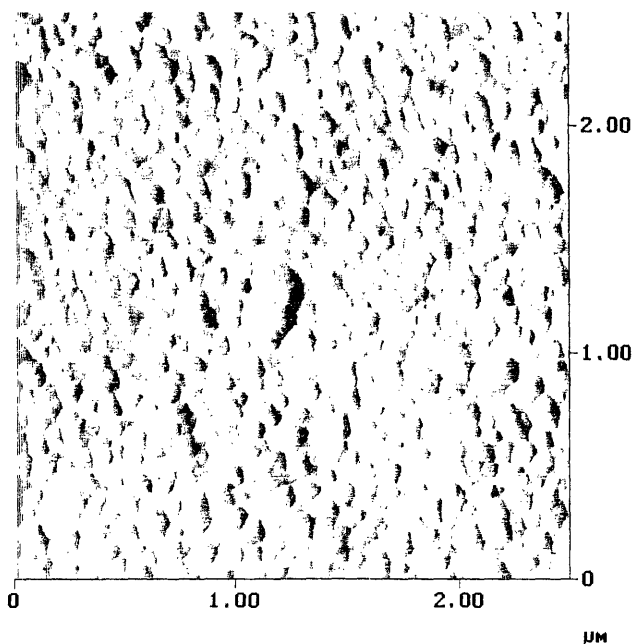


Fig. 31: AFM image (30 μm) of nucleation site (center) of a platelet

sometimes observable at the junction between three platelets, hinting at the fact that growth of the platelets has stopped before complete filling of the space surrounding them.

Smaller features called nanoasperities can also be seen on Fig. 30 and 31. They appear in the form of rounded bumps and cover the entire surface of the platelets with the

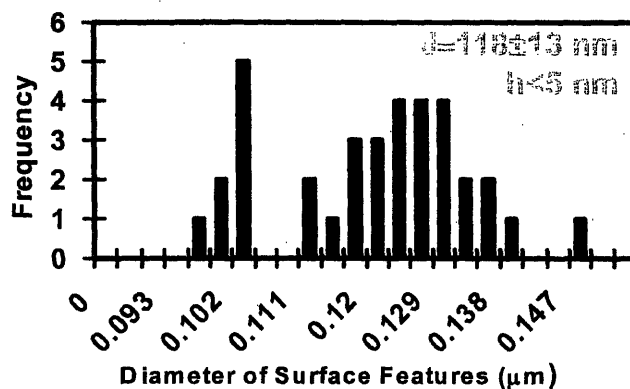


Fig. 32: Distribution of the diameters of the nanoasperities

same density, regardless of the region. Fig. 32 shows the width repartition of 34 nanoasperities on the surface of a platelet. The average “diameter” was found to be 118 ± 13 nm, and the height of 4.6nm in average.

Finally, we could observe that in-plane layers are not always distinct from their lower and upper neighbors, as displayed in Fig. 33. Here, the same brick is shared by to superimposed layers. Such defects remind the shape of a screw dislocation, an order of magnitude bigger. Fig. 34 is a zoom on the border of a platelet, showing a very regular profile. The edge itself seems to exhibit some remains of the matrix.

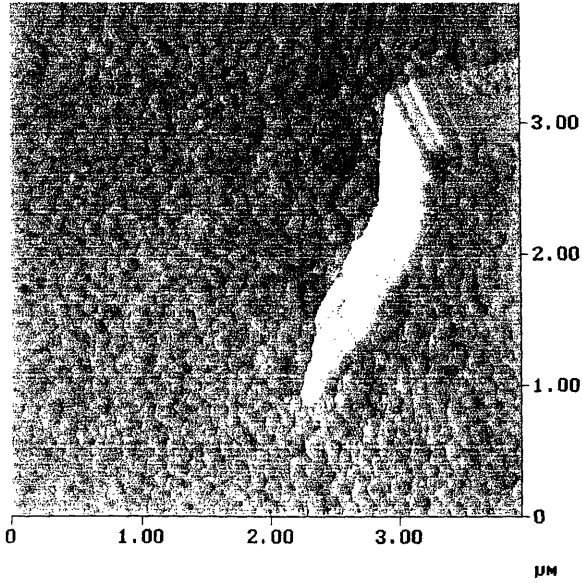


Fig. 33: AFM image (4 μm) of the partial edge of a brick shared by to stacked layers

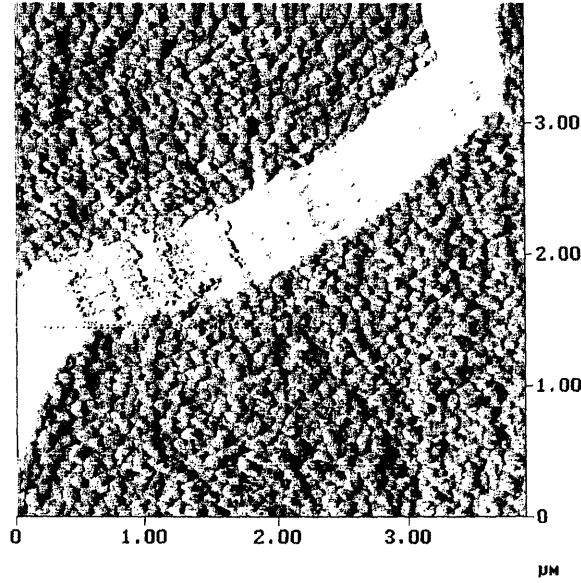


Fig. 34: AFM image (4 μm) of the edge of a brick lying on a nacreous layer

Three-point Bending Tests

Load versus deflection distance curves from multiple experiments were averaged and standard deviations calculated and presented on the plots (Fig. 36 and 37). The fairly low standard deviations stress the homogeneity of the results. The mechanical properties are summarized in Table 2 for dry and wet nacre respectively:

	E (GPa)	σ_f (MPa)	ε_f (%)
Dry nacre	68.0 ± 11.4	231 ± 34	4.0 ± 1.6
Wet Nacre	65.4 ± 9.6	213 ± 42	7.2 ± 1.0

Table 2: 3-point bending properties of dry and wet nacre

Results show the existence of large strain nonlinearities for the wet samples, whereas the behavior is mainly elastic before fracture for the dry samples. The Young modulus remained relatively constant (65.4 (wet) vs. 68.0 GPa (dry), 4% change), the true fracture strength dropped by 8% (231 vs. 213 MPa) and the true strain at fracture increased by nearly 80% (7.2 vs. 4.0 %). Thus dry nacre appears to be slightly stronger and stiffer in bending, while wet nacre exhibits much more ductility and toughness.

Uniaxial Compression Tests

The breaking fashion happened to be very different depending on the orientation of the layers versus the load. In the case where the layers were perpendicular to the load, final breakage occurred as burst of the whole sample in thin particles (10~500 μm). In the case where they were parallel to the load, the sample would eventually nicely cleave in two or

Trocha 3-point Bend Test - Dry Samples

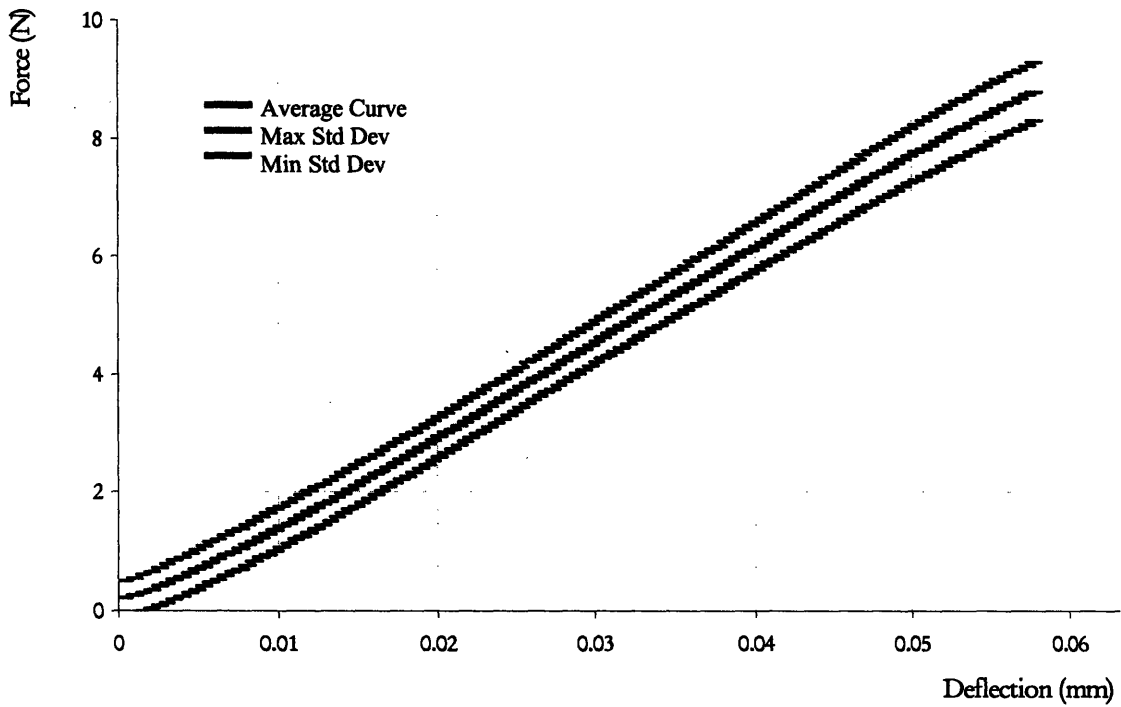


Fig. 35: Averaged Load versus Deflection curves from 3-point bend testing of dry nacre

Trocha 3-point Bending - Wet Samples

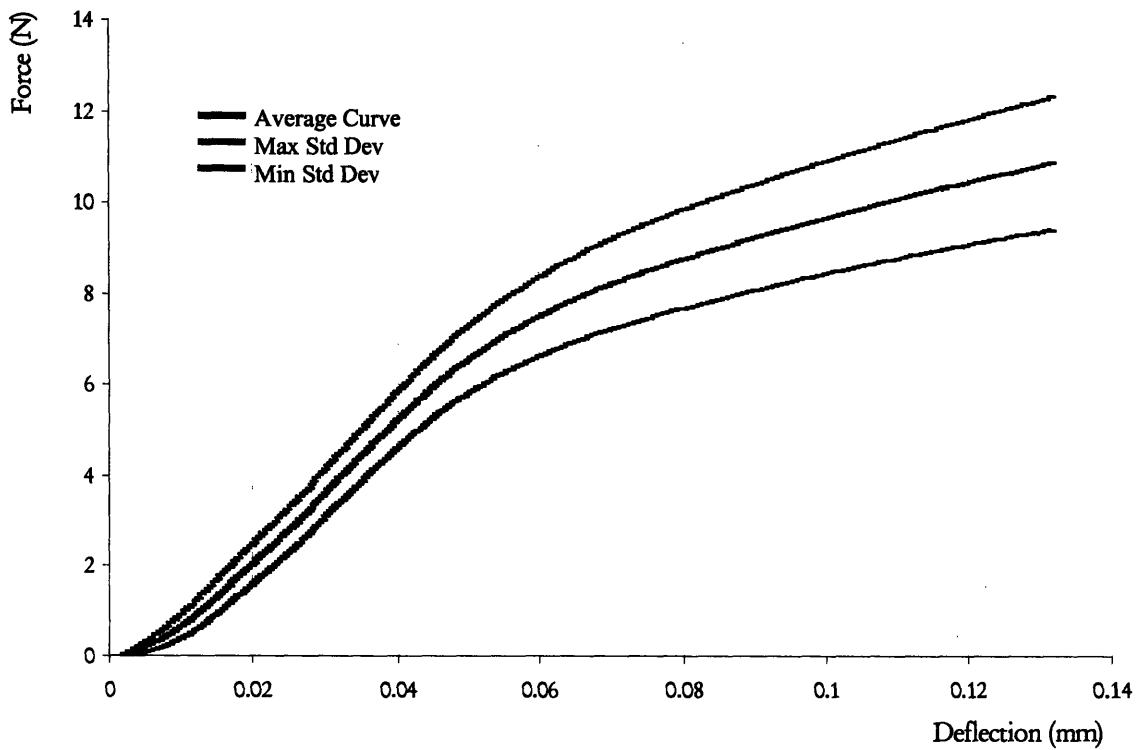


Fig. 36: Averaged Load versus Deflection curves from 3-point bend testing of wet nacre

more pieces along the planar nacreous layers (see previous chapter).

True stress-strain curves from multiple experiments were averaged and standard deviations calculated and presented on the plots (Fig. 38 and 39). The fairly low standard deviations stress the homogeneity of the results. Numerical applications gave the results below (Table 3), for dry and wet nacre respectively:

Orientation	E (GPa)	σ_f (MPa)	ε_f (%)
Parallel to force	63.8 ± 14.7	225 ± 44	0.55 ± 0.05
Perpendicular to force	19.1 ± 3.4	663 ± 71	3.3 ± 0.3

Table 3: Compression properties of nacre relative to layer orientation

Great differences in the mechanical properties were recorded according to the orientation of the nacre layer: Young modulus (63.8 (parallel) vs. 19.1 GPa (perpendicular), fracture strength (225 vs. 663 MPa), strain to failure (0.55 vs. 3.3 %). Thus nacre appears to be stiffer in-plane, but much tougher and stronger across the plane. The discrepancy between the moduli emphasizes that very distinct deformation mechanisms prevail during these tests, which is confirmed by the fact that fracture occurs also in three different ways: through thickness and interlaminar and “burst” respectively.

Trocha Compression Tests - Layers parallel to the load

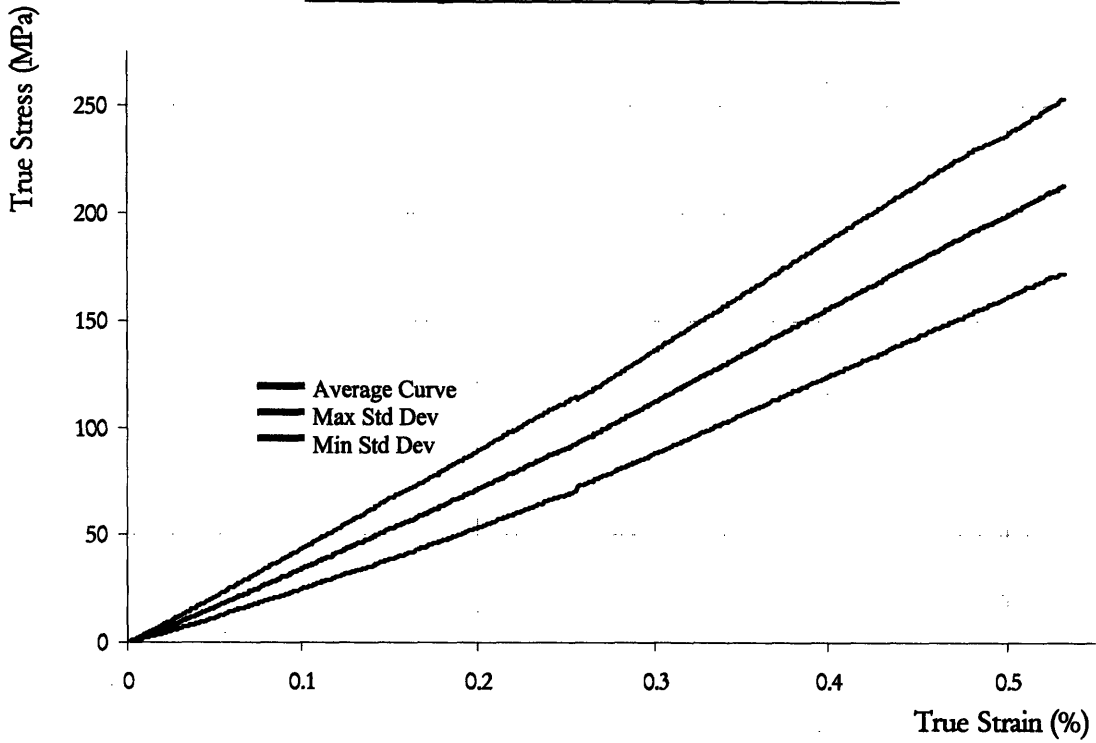


Fig. 37: Averaged Stress versus Strain curves from compression testing of nacre with the layers parallel to the load

Trocha Compression Test - Layers perpendicular to the load

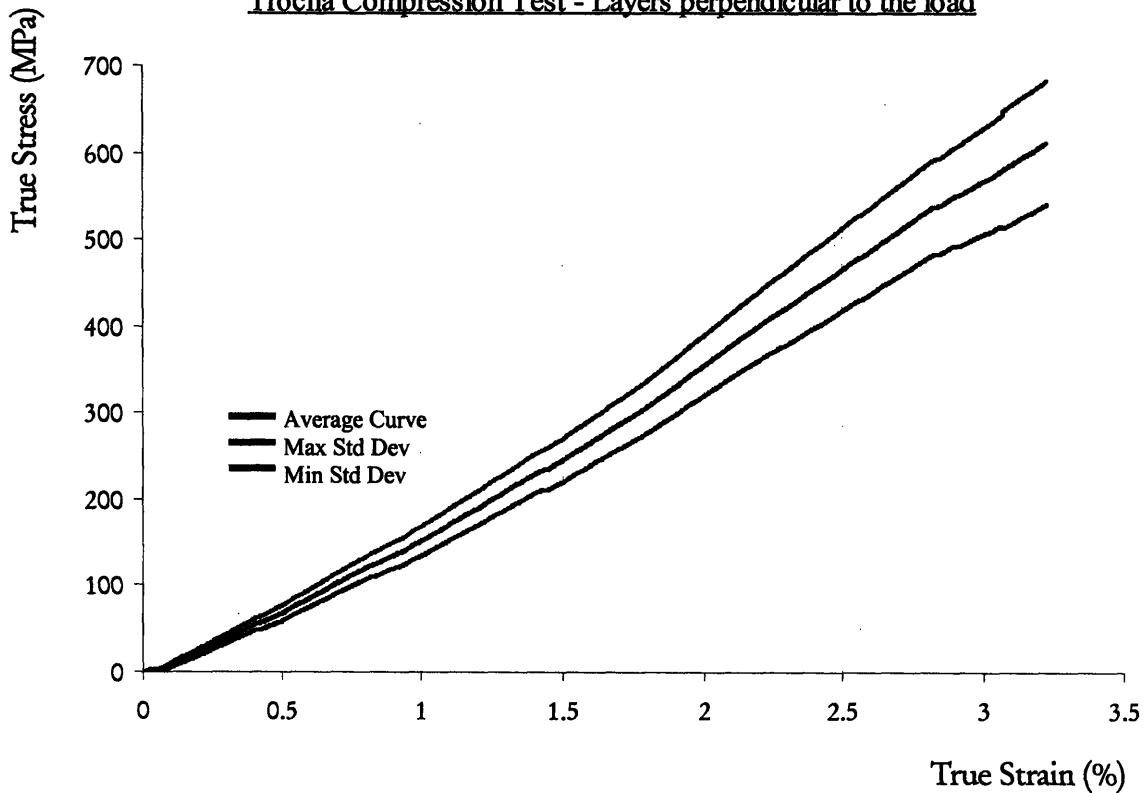


Fig. 38: Averaged Stress versus Strain curves from compression testing of nacre with the layers perpendicular to the load

Observation of Fractured Regions after Macromechanical Testing

SEM and AFM were used to characterize deformation mechanisms at the microscopic level upon 3-point bend and compression testing. As described in the previous section, only the compression samples with layers parallel to the load cleaved in the form of flat layers and could thus be imaged.

1. Fractured Regions in 3-point Bending Samples

The observation of the fractured zone (more or less along the cross-section) of broken samples showed that different fracture mechanisms take place within the material.

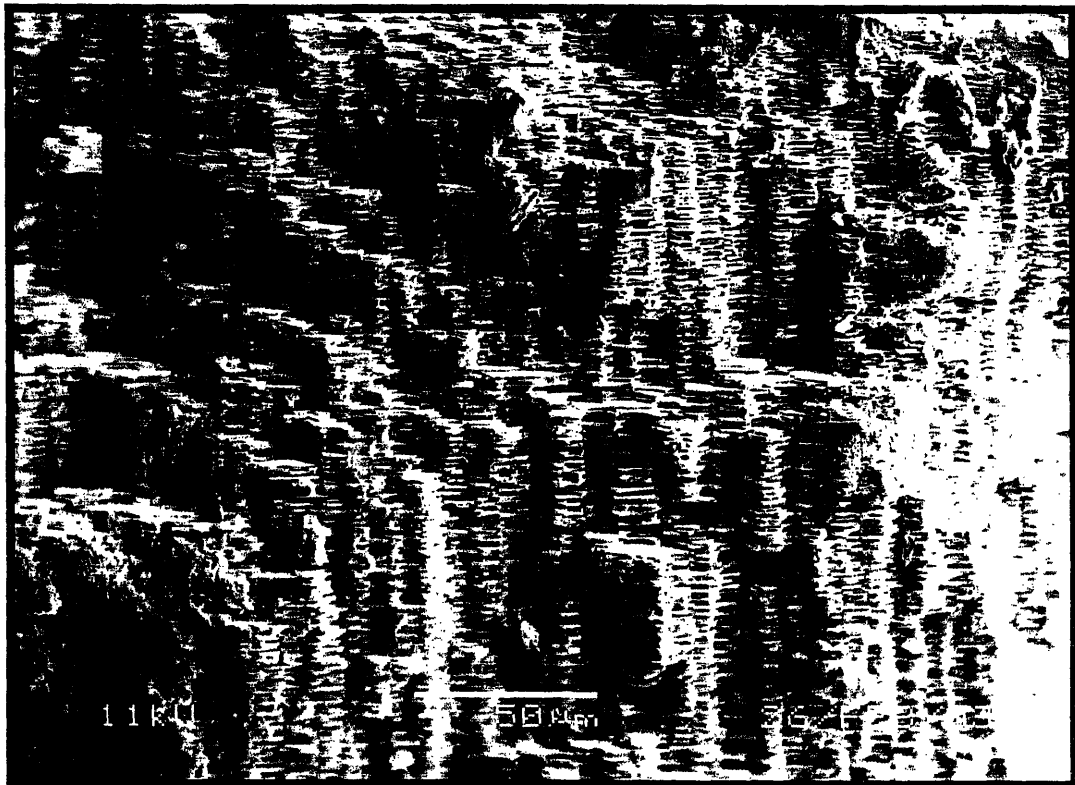


Fig. 39: SEM image (300 μm) of the fracture surface of a broken 3-point bending sample

Fig. 40 illustrates the very irregular path of the main crack across the sample, randomly cutting through the columns of platelets. Stacks of platelets are either run around or cut perpendicularly to their axis by the crack. Most of the bricks appear intact, but the presence of some pieces chipped away is a hint that some of the platelets are actually broken during fracture.

The cracks appear as combinations of deflections both at the column and brick length scales. A quantitative analysis of the images indicates that the cracks undergo a major change in direction every 40 μm , but is typically deviated every 500 nm at the brick level. Bricks pulled out of the structure can also be seen on Fig. 40.

2. Fractured Region in Compression Samples

As in 3-point bend tests, the observation of cleaved compression samples revealed the existence of numerous deformation mechanisms.

Analysis of Fig. 41 led to the following observations: in-layer cracks virtually always follow the outline of bricks and thus they kink every 5 nm in average. Length of cracks varies from ten to hundreds of nanometers. Short cracks can be very tortuous, intricate and branch every 15 nm in highly fractured regions as in Fig. 42. Main cracks have a more constant orientation (Fig. 41 and 43).

On Fig. 43, we can identify jagged and branched crack fronts at plate interfaces. The straightest cracks always display a minimum amount of kinking, weaving around the platelets. Fig. 44 shows the presence of debris from broken platelets.

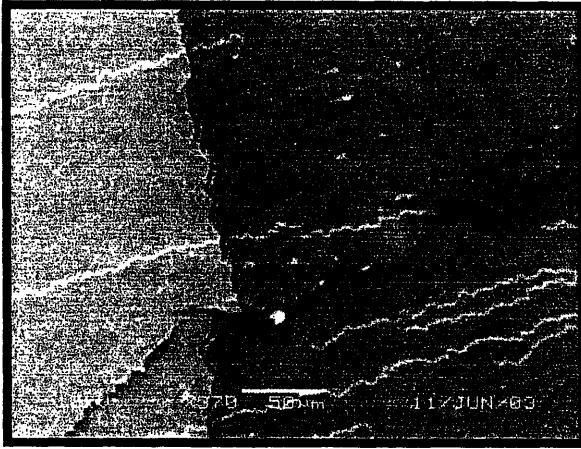


Fig. 40: SEM image (350 μm) of columnar microstructure

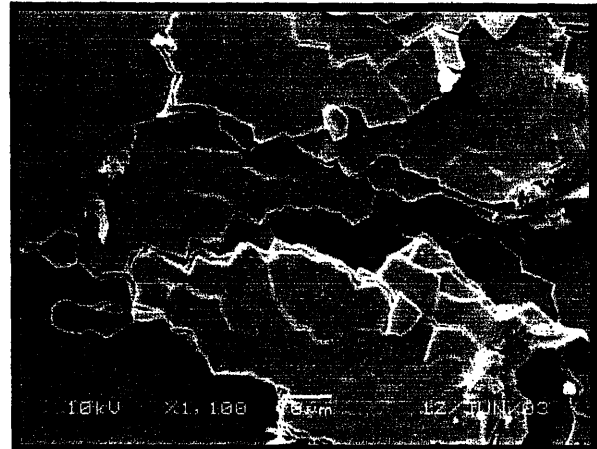


Fig. 41: SEM image (100 μm) of columnar microstructure

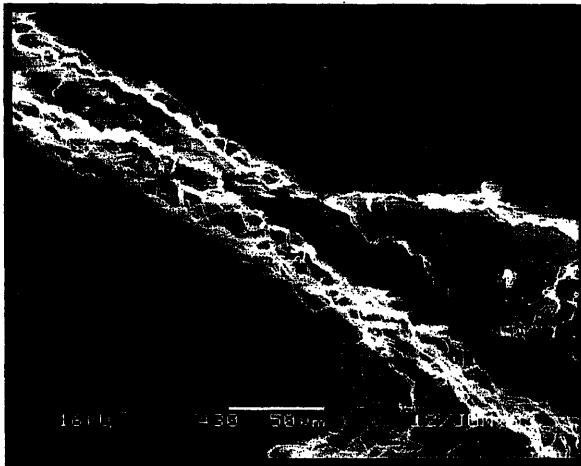


Fig. 42: SEM image (300 μm scan) of a large through-thickness crack

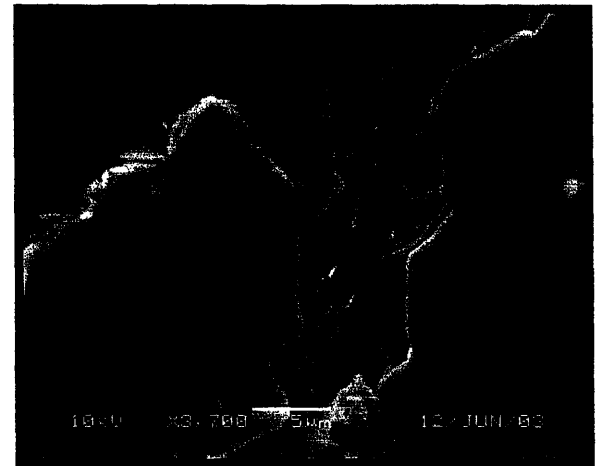


Fig. 43: SEM image (30 μm scan) of a small through-thickness crack

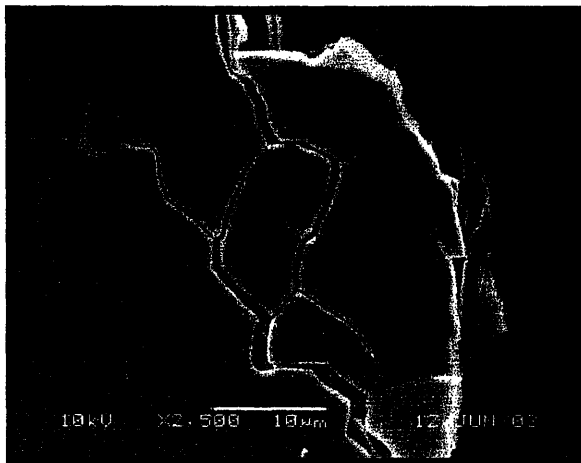


Fig. 44: SEM image (50 μm scan) of in-plane branched microcracks

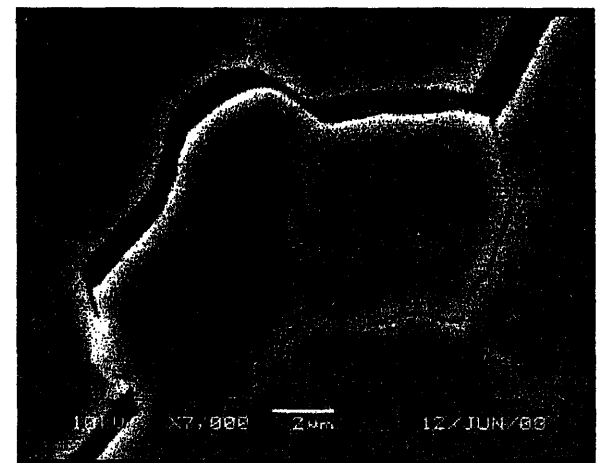


Fig. 45: SEM image (15 μm scan) Detail of a microcrack

Polygonal "holes", curved crack path, non-uniform angles of polygons can be observed on Fig. 45 and 46.

AFM imaging proved to be less convenient than SEM as very steep slopes or drops bigger than 100 nm are not accurately rendered. Nevertheless, some details of interest could be imaged: on Fig. 47, the appearance of the superimposed layers

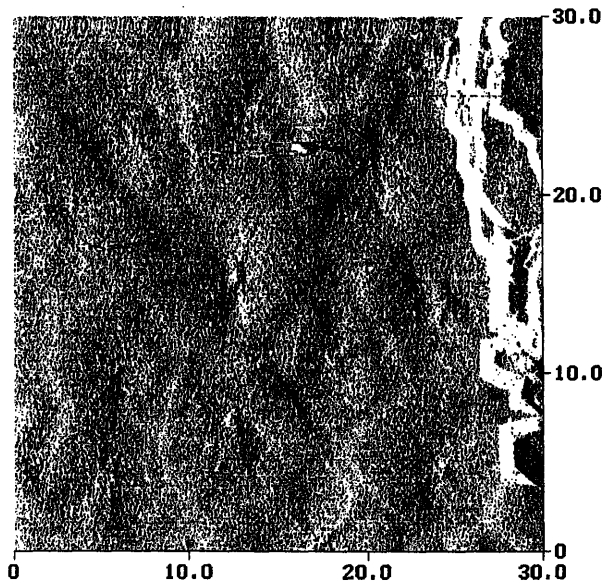


Fig. 46: AFM image (30 μm scan) of fractured nacreous layers superimposed

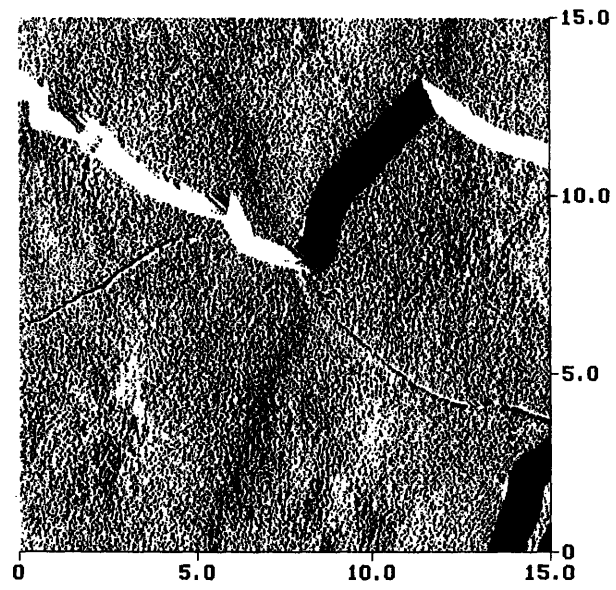


Fig. 47: AFM image (15 μm scan) of a cracked edge and microcrack running between platelets

correlates well with the SEM observation of broken 3-point bending samples. It can be seen that platelets of a same stack overlap each other only imperfectly. On Fig. 48, we can notice that the edge of the upper layer has a very sharp profile, and the irregular appearance of the right edge could indicate a breakage. On the lower layer, one can perceive a narrow crack running through otherwise intact platelets. Its width is not greater than 200 nm and it follows perfectly the outlines of the surrounding bricks.

Nanomechanical Testing

Fig. 50 and 51 are overlay plots of the average nanoindentation curves at a different maximum loads, comparing all three types of samples. Standard deviations were also calculated and the plots display the maximum values for each series in the form of error bars. In the following description of the results, the different curves will be referred to using their peak load value and the sample tested. The Oliver-Pharr method¹⁶ was used to calculate the Young moduli and the hardnesses.

From Fig. 50 it can be seen that the average loading responses of the three different types of samples already diverge at the smallest loads. The comparison of the 50 μN curves shows that fresh nacre exhibits very little plasticity, with a permanent deformation of ~ 3 nm (depth of the indent upon total unloading) in average. This is less than a third of the permanent deformation induced in wet nacre (~ 10 nm), and about half of the one in calcite. These results correlate well with the hardness distribution at 50 μN (Fig. 53), which gives an indication of the plasticity of the material (respectively 4.49 ± 0.98 and 3.06 ± 1.47 GPa for calcite and wet nacre). The Young modulus (Fig. 52) of dry nacre appears to be bigger in average to those of wet nacre and calcite, but could not be retrieved for the 50 μN curve for dry nacre, because of a singularity in the area tip function at depths smaller than 10 nm.

The 100 μN curves show an inverted trend for wet nacre and calcite. While dry nacre still has the stiffest and less plastic response, we observe that calcite now has a higher degree of plasticity than wet nacre. This is confirmed by the hardness values, almost constant (4.41 ± 0.52 GPa) for calcite, much higher (7.03 ± 1.57 GPa) for wet

nacre. The difference between the three Young moduli tends to be smaller.

For loads of 250 μN up to 1000 μN , it can be seen that dry nacre remains the stiffest and the less plastic. The hardness of wet nacre lies in between those of dry nacre and calcite, and the distribution is quite broad ($\sim 11, \sim 8, \sim 3$ GPa for dry nacre, wet nacre and calcite respectively) . The Young moduli are more similar: all the values are comprised between 100 and 130 GPa, with the calcite value lying in-between those of dry and wet nacre. Table 4 summarizes the Young moduli, hardnesses and maximum indent depths for the 1000 μN curves.

	E (GPa)	H(GPa)	h_{max} (nm)
Dry nacre	112.3 ± 9.2	10.5 ± 1.6	67.7 ± 3.2
Wet Nacre	100.1 ± 10.6	8.2 ± 1.5	73.8 ± 4.6
Calcite	102.6 ± 3.1	3.2 ± 0.1	97.6 ± 1.5

Table 4: Nanoindentation properties of dry nacre, wet nacre and calcite (1000 μN max load)

For calcite, individual curves were relatively smooth with no discontinuities or distinct changes in slope apparent. On the contrary, both dry and wet nacre curves showed sudden steps or brief changes in the slope during the loading part (Fig. 49).

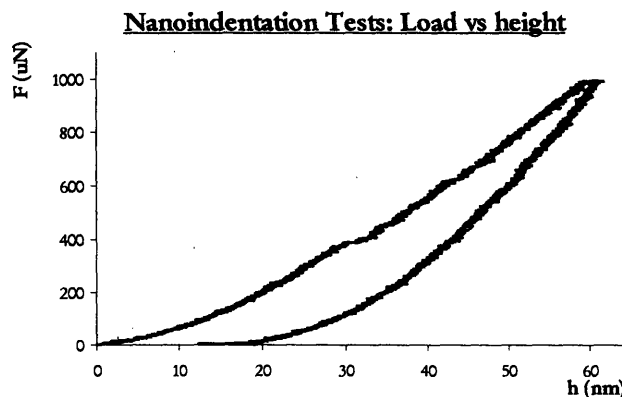


Fig. 48: Single Load vs. Indentation Depth curve during nanoindentation testing of dry nacre

Nanoindentation Tests: Load vs height

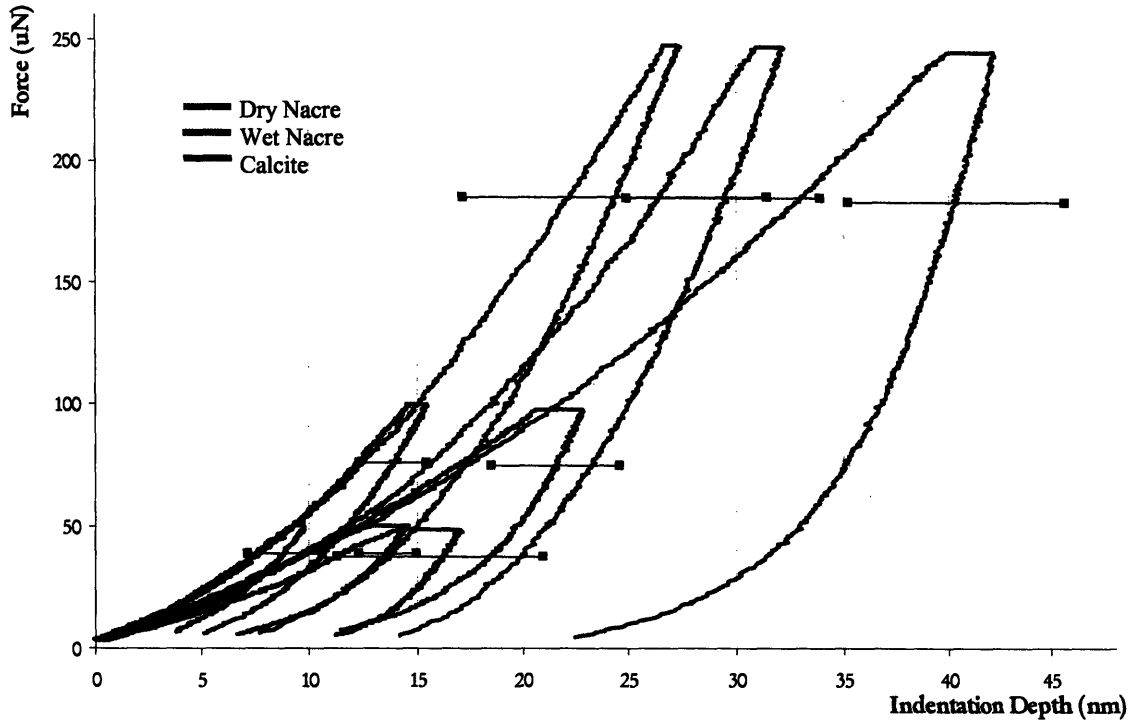


Fig. 49: Averaged Load (50 to 250) vs. Indentation Depth curves from nanoindentation testing of dry nacre, wet nacre and calcite

Nanoindentation Tests: Load vs height

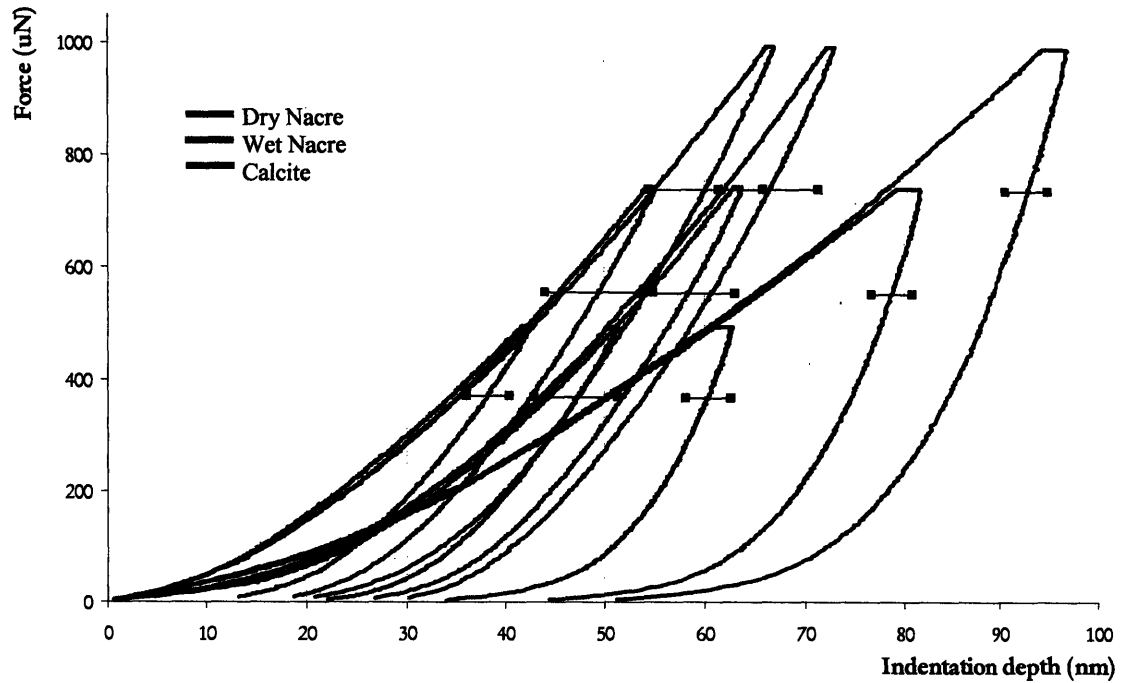


Fig. 50: Averaged Load (500 to 1000) vs. Indentation Depth curves from nanoindentation testing of dry nacre, wet nacre and calcite

Nanoindentation tests: Young Moduli versus Peak Load

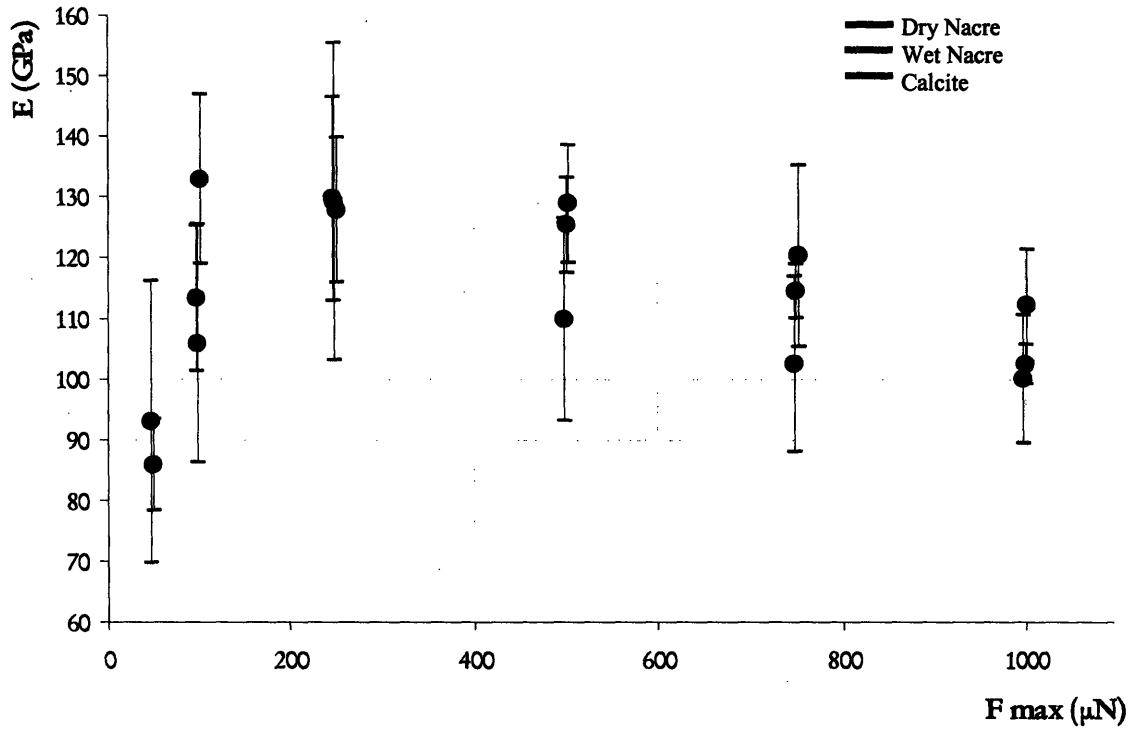


Fig. 51: Averaged Young Modulus calculated from nanoindentation curves of dry nacre, wet nacre and calcite

Nanoindentation tests: Hardness versus Peak Load

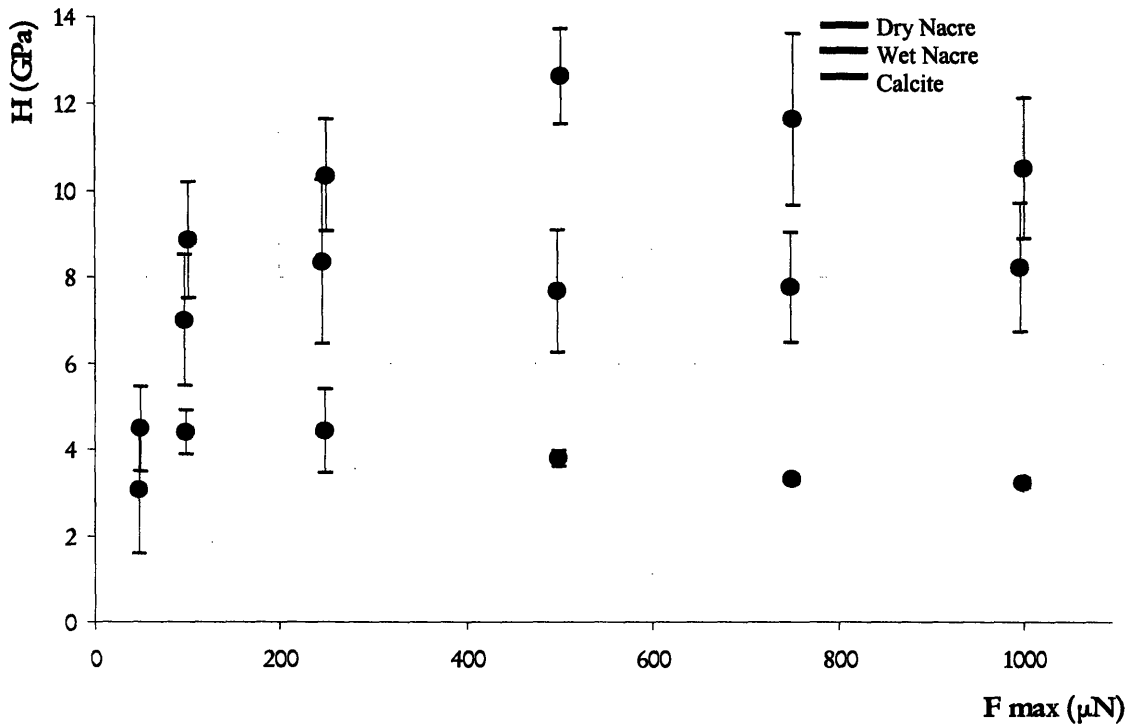


Fig. 52: Averaged Hardness calculated from nanoindentation curves of dry nacre, wet nacre and calcite

Observation of Indented Regions after Nanomechanical Testing

Fig. 54 and 55 are a Tapping Mode AFM image (*Q-scope*) of the indented region of respectively dry and wet nacre samples. The images presented here are from higher loads indents (between 5 and 9 mN), in order to provide a better insight in the characteristics of the deformation. At smaller loads, the deformation induces similar features but of smaller size. However, under 100 μN it is hard to image the footprint, since plastic deformation is less important and because of the somewhat imprecise positioning of the integrated AFM.

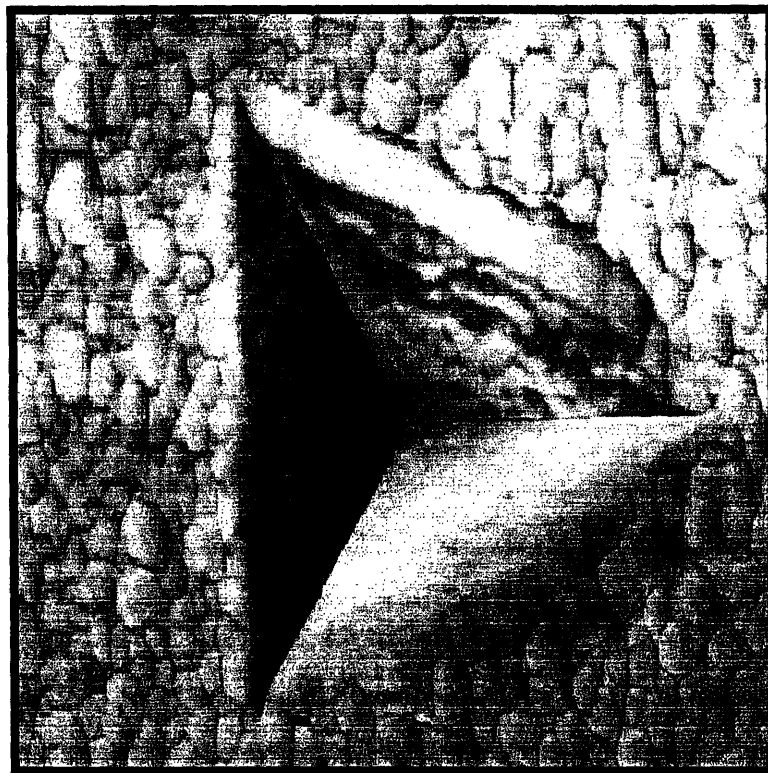


Fig.53 : AFM image in air (2.5 μm scan): 9 mN indent mark on a platelet surface (dry nacre)

On both Fig. 54 and 55, residual deformation is clearly visible localized within

the indent region whereas the material away from the indent region looks unchanged. This extensive plastic deformation within the tablet is particularly significant for soaked nacre. Pile-up took place along the borders of the indent, with a height relative to undeformed region of 45 ± 20 nm and 60 ± 20 nm for a 9mN load in dry nacre and a 5mN load in soaked nacre respectively. Each pile-up zone extended out by 400 ± 200 nm

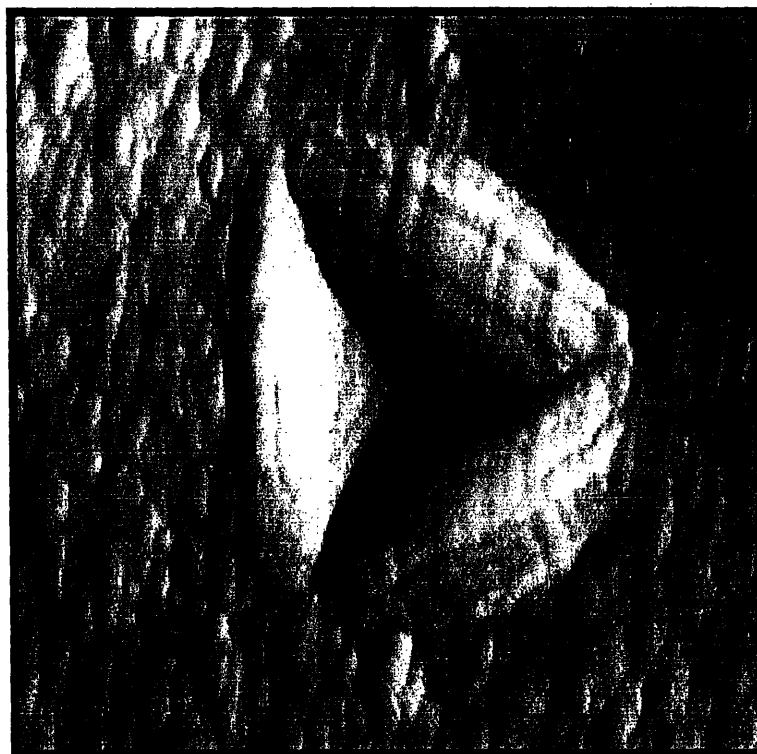


Fig. 54 : AFM image in air (3 μ m scan): 5 mN indent mark on a platelet surface (wet nacre)

and 500 ± 200 nm respectively from the indent border and the surface area it covered was of $0.5 \pm 0.2 \mu\text{m}^2$ and $0.7 \pm 0.2 \mu\text{m}^2$ respectively. In the indented region, a morphological change is also visible. Stripped zones with a width similar in average to the one of the nanoasperities are observable, which let us think that nanoasperities have been flattened

(rms roughness divided by 2 to 10 from the borders to the center of the indent).

On the other hand, no brittle microcracks could be detected, even at greatest magnification available with the AFM ($\sim \times 1,000,000$) and no plastic deformation was detectable away from the indented region.

DISCUSSION

3-point Bend Tests

In the literature, the 3-point bend modulus of sheet and columnar nacre (*Pinctada* and Abalone shells respectively) has been found^{1,3} to be around 70 GPa (dry nacre) and 60 GPa (wet nacre), which correlates well with the values of respectively 68 and 65.4 GPa that we measured for *Trochus Niloticus*. Tensile strengths have been measured^{1,5} to be close to 170 -180 MPa (dry nacre) and 140 MPa (wet nacre). Again, this compares well with the values determined here, 231 and 213 MPa respectively. Fig. 36 and 37 are also consistent with the observation¹ that hydration of nacre increases both ductility and toughness.

As shown in Fig. 40, the platelets appear mostly intact, but some broken pieces are nevertheless observable, indicating that, for the crack path, a competition exists between walking around and cutting through the bricks. This highlights how well calibrated nacre is. However, if the highly tortuous fracture surface upon 3-point bend tests is an obvious toughening effect of the brick and mortar structure of nacre, the fact that the work of fracture of nacre is about 3000 times greater than the one of pure aragonite^{1,2} is principally due^{1,3-6} to sliding of the bricks along each other caused by

tensile stress, leading to bridging of the organic matrix, as can be seen on Fig. 21. Beside the ligament formation, the elastic compression of nanoasperities during sliding of the bricks has also been shown^{3,15} to play a great role in the nonlinear deformation of nacre. These mechanisms are believed to absorb most of the strain energy while maintaining cohesion in the microstructure. Delamination is another toughening mechanism, but mostly occurs in wet nacre¹, presumably because of the greater stiffness of the organic matrix. Water thus enhances the toughness of nacre, by allowing greater plasticity to the organic layer.

Compression Tests

From the literature^{3,16}, the shear modulus of columnar nacre has been found to be about 8GPa (columnar nacre), while the Young moduli of sheet nacre were measured to be of 40 GPa and 20 GPa, with the load parallel and perpendicular to the layers respectively. The compressive strength was about 235 and 540 MPa respectively. Our results compare well for the compressive strengths as well as for the “across” in-plane compression test. However, the “in-plane” Young modulus of 63.8 GPa found in this work is 50 percent higher. A possible explanation lies in the differences in the size of the bricks and the organic layer between the two shells.

Concerning the way the material deals with the loading mode, we can try to understand the overall tendencies in the deformation of the layers. For loading parallel to the layers, the intrinsic irregularities of the compressed surface (perpendicular to the platelets edges) promote interlamellae slip to homogenize the stress repartition. Similarly

the overlaying sheets will have a tendency to buckle due to their large area compared to their thickness, finally leading to the observed interlaminar failure (Fig. 22). Such a failure mode cannot exist when loading is perpendicular to the layers, as it compresses in an homogeneous manner the overlaying sheets of nacre. The early stages of compression affect mostly the soft organic layer, which transfers the load to the bricks when it reaches its plastic region. The conversion of compressive stress to tensile stress by the ceramic platelets then eventually leads to lateral burst of the whole material, as observed in the tests.

Nanoindentation

Some experiments of micro/nanoindentation of shells have been recently related^{17,18} in the literature, but never on columnar nacre in the range of 100-1000 μN . Nanoindentation of thermally etched *Haliotis Rufescens* (Red Abalone) aragonite bricks shows¹⁷ an elastic behavior for depths and loads up to 45 nm and 150 μN respectively. A transverse modulus of 82 GPa and an in-plane one of 107 GPa was reported for nacreous aragonite. Two stages were observed when loading, the first stage from zero force up to 30 nm/30-40 μN (high compliance), apparently due to the flattening of nanoasperities; the second stage from 30nm/30-40 μN up to 45 nm/150 μN , exhibiting a much higher Young modulus corresponding to the elastic domain of nacreous aragonite. Simulations of indentation of pure aragonite grains transversely isotropic yielded the following experimental data points just before unloading: 8 nm/50 μN , 13 nm/100 μN , 25 nm/250 μN , which are very consistent with our curves. However our results indicate that natural

nacre already exhibits plasticity at 50 μN , even if limited. Also, we cannot distinguish two stages on our curves, but rather a transition region with increasing stiffness followed by a second region of more constant stiffness. Thus the presence of the organic layer seems to play a role in the plasticity of nacre at small loads, as well as contribute to a more even distribution of the load on the surface of the platelet. In this case, the flattening of nanoasperities, also observed on Fig. 54 and 55 is carried out in parallel of the actual compression of the platelet, rather than occurring before.

In another article¹⁸, micro/nanoindentation of the shell of Pectinidae (crossed lamellar structure) yielded a hardness of 5 ± 0.3 GPa and Young Modulus of 87 ± 5 GPa for indentation loads and depths ranging from 100 to 800 μN and ~ 15 to 90 nm respectively. Nevertheless, the value of the Young moduli and hardnesses are very consistent only from 27 nm/200 μN and above, as noticed for our experiments. Considering only the higher loads on Fig.51, we see that for Trochus Niloticus the modulus of dry nacre is about 120 GPa and its hardness about 12 GPa. The discrepancy with the absolute values found for Pectinidae can be explained by the difference in the microstructure (columnar vs. crossed lamellar) as well as in the nanostructure (shape and mineral/organic content of the platelets).

Nevertheless, these values are much higher than the macroscopic value of 19.1 GPa obtained by macroscopic uniaxial compression where the load direction was perpendicular to nacre plate axis, similarly as during the nanoindentation tests. The nanoscale Young modulus value is much closer to the Young modulus of pure aragonite (88.2 GPa) than to the macroscopic one. This suggest that deformation during macroscale

compression is mostly felt by the organic matrix, as we explained in the previous section, while both elastic and plastic deformations during nanoindentation are mostly sustained by the mineral component, at least for loads bigger than 100 μN . As for the Young Modulus being higher than the one of pure aragonite (120 vs. 88.2 GPa), the moduli that fits to nanoindentation data have been observed to usually exceed those measured by macroscopic mechanical measurements for other types of other materials as well¹⁹. Differences in the loading rates and/or data analysis used can also contribute to discrepancies in the results.

The difference in the values observed on Fig. 52 and 53 for both moduli and hardnesses depending on the peak load or, similarly, on the maximal depth of indentation, can be explained by several arguments. First, nacre being a composite, this can be the indication that this material cannot be approximated as homogeneous at the nanoscale. This correlates well with the fact that the surface of a platelet is coated with ~ 40 nm of organic matrix. It is unfortunately difficult to quantify how much of this organic layer is still present after exposure to air for a few hours, since nanoindentation tests lasted approximately 26 hours. For that reason, testing at higher loads (above 100 μN , where the organic response is less significant) ensures a better consistency. Second, the fact that loads below 100 μN did not yield moduli that can be considered as accurate is mainly due to the non-ideal tip shape. As a matter of fact, the only 6 coefficients used to fit the area-depth function of the tip used in the Oliver-Pharr method are not sufficient to render the critical details of the tip shape. Enhanced simulation methods, like FEM, are necessary to model more accurately the behavior of the tip at very low indent depth. And third, the use

of a different loading rate (not mentioned in [18]) can also be a reason for the discrepancy in the results.

Concerning the dry and wet states of nacre, the average moduli value calculated from O-P analysis for dry nacre was found to exceed the one of wet nacre by ~ 10% which is consistent with the trend for macroscopic tensile modulus of nacre, known to decrease with the water content¹.

Lastly, another interesting fact lies in the observation that for greater loads (1 to 10 mN), discontinuities in the experimental curves can be explained by sudden displacements of tablets relative to its neighbors as it is indented (Fig. 49). This additional mechanism can contribute to a drop in the Young Modulus and yield values closer to the macroscopic one.

CONCLUSION

In this paper, a multitechnique experimental methodology is presented for studying multiscale mechanical properties and detailed deformation mechanisms of nacre that has been subjected to minimal sample preparation yielding closer to physiological conditions. We apply this methodology to a series of model samples to study the effect of water content, which is one important parameter known to influence the toughness of nacre. Fresh and hydrated nacre samples were prepared, characterized, and tested by 3-point bending, uniaxial compression and nanoindentation.

The study of the inner columnar nacreous layer from the shell of *Trochus Niloticus* showed that this biocomposite has a multiscale hierarchical structure. At the microscale this material is organized in superimposed layers of small platelets (~ 6 μm long, ~ 800 nm thick). The platelets are vertically stacked and their nucleation sites coincide with the one of their upper and lower neighbors. At the nanoscale, it is found that each tablet is made of one or more aragonitic sectors, separated by organic walls along radii drawn from the nucleation site to the outlines of the tablet. This organic matrix, made of different varieties of proteins, also surrounds every platelet and acts as an

adhesive. The surface of the tablets exhibit a roughness due to nanoasperities (~ 120 nm in diameter)

Macroscopic 3-point bend tests yielded an in-plane Young modulus of 68 GPa and 65.4 GPa for freshly cut samples and samples soaked for 10 weeks respectively. A fracture strength of 231 MPa and 213 MPa respectively was measured. Samples soaked for 10 weeks, exhibited major non-linearities in the stress-strain curves, emphasizing the greater toughness of hydrated nacre. Uniaxial compression yielded Young moduli of 63.8 GPa for samples with the brick layers oriented parallel to the load, 19.1 GPa when oriented perpendicular to it and fracture strengths of respectively 225 and 663 MPa. The discrepancy between the compression moduli emphasizes that very distinct deformation mechanisms prevail during these tests, which is confirmed by the fact that fracture occurs in three different ways (respectively through thickness, interlaminar and shatter). Scanning electron microscopy (SEM) and AFM of fractured samples revealed jagged and branched crack fronts at plate interface, tortuous crack paths, non-uniform angles of polygons (suggesting possible intrinsic deformability and displacement/sliding).

The technique of *nanoindentation* was carried out on individual aragonite tablets using a diamond-coated Berkovich probe tip (end-radius of 70 nm, tip angle of 142.3 degrees), at a rate of indentation of 10 $\mu\text{N/s}$ (load controlled), forces from 10 to 1000 μN and indentation depths from 10 to 97 nm. AFM inspection of the indented region showed the existence of extensive plastic deformation within the tablet and suggested that occluded biomacromolecules may play a significant role in the deformation at loads

below 100 μN . Using the contact elastic theory, a Young modulus of 112.3 GPa and a hardness of 10.5 GPa were found for an individual platelet.

This work aimed at assessing and understanding the surprisingly good mechanical properties of a material composed 95% wt of calcium carbonate, and only a few percent of an organic matrix, Further investigation of the nanoscale deformations mechanisms will require a more precise knowledge of the composition, localization and nanoscale mechanical properties of the organic constituents, through physical and biochemical characterization. Finite Element Method simulation of the nano/microscale behavior will also be used to quantitatively link the multiscale phenomena at the origin of the outstanding mechanical characteristics of nacre.

APPENDIX

THE OLIVER-PHARR ANALYSIS METHOD

The procedure used to determine the reduced Young's Modulus E_r and the Hardness H of the material from nanoindentation curves is described below. The portion of the unloading curve between 95 and 20 % of the maximum load is fit to the power law relation,

$$P = B(h - h_{\max})^m$$

where

P is the load

B is a constant to be determined

h is the indentation depth

h_{\max} is the maximal indentation depth

m is a constant to be determined

The derivative of the power law relation with respect to h is evaluated at the maximum load to calculate the contact stiffness S ,

$$S = \left(\frac{dP}{dh} \right)_{h_{\max}}$$

The contact depth, h_c , is calculated with the following equation:

$$h_c = h_{\max} - \frac{3P_{\max}}{4S}$$

The hardness H is calculated with:

$$H = \frac{P_{\max}}{A(h_c)}$$

where $A(h_c)$ is the projected contact area of the tip at the height h_c . Practically, the area function is calibrated before each set of experiments (see below).

The reduced modulus (see definition below) is calculated with:

$$E_r = \frac{\sqrt{\pi}}{2\sqrt{A(h_c)}} S$$

Tip-shape calibration is based on determining the area function of the indenter tip. The method is based on the assumption that Young's modulus of elasticity is constant and independent of indentation depth. Fused quartz with reduced Young's modulus of 69.6 GPa is used as a standard sample for calibration purpose. An area function relating the projected contact area (A) to the contact depth (h_c) is obtained. For an ideal pyramidal geometry Berkovich tip, the projected contact area to depth relationship is given by:

$$A(h_c) = 24.5h_c^2$$

In the general case,

$$A(h_c) = \frac{\pi}{4} \left(\frac{S}{E_r} \right)^2$$

where the reduced modulus E_r accounts for the fact that the measured displacement includes contribution from both the specimen and the indenter. The reduced modulus is given by:

$$\frac{1}{E_r} = \left(\frac{1-\nu^2}{E} \right)_{specimen} + \left(\frac{1-\nu^2}{E} \right)_{indenter}$$

where E and ν are the elastic modulus and Poisson's ratio of the specimen and the indenter respectively.

To determine the area function, a series of indents at various contact depths (normal loads) are performed on fused quartz specimen and the contact area (A) calculated using the general equation above. A plot of the computed area as a function of contact depth is plotted and a fitting procedure is employed to fit the (A) versus (h_c) to a sixth order polynomial of the form:

$$A(h_c) = C_0 h_c^2 + C_1 h_c + C_2 h_c^{1/2} + C_3 h_c^{1/4} + C_4 h_c^{1/8} + C_5 h_c^{1/16}$$

Adapted from TriboScope® Users Manual, © 2003 Hysitron Inc.

REFERENCES

- (1) Jackson AP, Vincent JFV, Turner RM: "The mechanical design of nacre" 1988 *Proc. of the Royal Soc. of London, Series B* **234**, pp 415-440.
- (2) Currey J. D., "Mechanical properties of mother pearl in tension", 1977 *Proc. of the Royal Soc. of London, Series B* **196**, Issue 1125, pp 443-463.
- (3) Wang RZ, Suo Z, Evans AG, Yao N, Aksay IA 2001 "Deformation mechanisms in nacre", *J. Mater. Res.* **16**[9], pp 2485-2493.
- (4) Sarikaya, M., and I.A. Aksay. 1992. "Nacre of abalone shell: A natural multifunctional nanolaminated ceramic-polymer composite material." Chapter 1 in *Structure, cellular synthesis and assembly of biopolymers*, ed. S.T. Case. New York: Springer-Verlag.
- (5) M. Sarikaya, K.E. Gunnison, M. Yasrebi and I.A. Aksay "Mechanical Property-Microstructural Relationships in Abalone Shell", *Materials Synthesis using biological Processes*, Proc MRS, **174** (Materials Research Society, Pittsburgh, 1990), pp 109-116.
- (6) M. Sarikaya, J. Liu and I.A. Aksay: "Nacre: Properties, Crystallography, Morphology and Formation". *Biomimetics, Design and Processing of Materials*. Ed M. Sarikaya and I.A. Aksay (1995).
- (7) Mutvei, H. "Ultrastructure of the mineral and organic components of molluscan nacreous layers". *Biomineralisation* **2**, pp 48-61 (1970).
- (8) Weiner, S. *CRC Crit. Rev. Biochem.* 1986, **20**, p 365.
- (9) D. Chateigner, C. Hedegaard & H.-R. Wenk, "Mollusk shell microstructures and crystallographic textures." *J. Structural Geology* **22**(11-12), 2000, 1723-1735.
- (10) Schäffer, T.E. *et al.* "Does Abalone nacre form by heteroepitaxial growth or by growth through mineral bridges?" *Chem. Mater.* **9**, pp 1731-1740 (1997).
- (11) Watabe, N. & Wilbur K.M. (eds) "The Mechanisms of Biomineralization in Invertebrates and Plants" *Univ. South Carolina Press*, Columbia, SC, 1976).
- (12) Smith, B. L. *et al.* Molecular mechanistic origin of the toughness of natural adhesives, fibres and composites. *Nature* **399**, pp 761-763 (1999).
- (13) Mutvei, H. "Ultrastructural Characteristics of the Nacre in some Gastropods." *Zool. Scr.* **7**, pp 287-296 (1978).

- (14) De Stefano, C. et al, "The single salt approximation for the major components of seawater: association and acid–base properties". *Chem Speciat Bioavail*, **10**, (1998) 27-30.
- (15) C. Ortiz, R. Kim, E. Rodiguero , C. K. Ober, and E. J. Kramer "Deformation of a Polydomain, Liquid Crystalline Epoxy-Based Thermoset", *Macromolecules* 1998, **31** (13), 4074-4088
- (16) Oliver, W.C. and G.M. Pharr, "An improved technique for determining hardness and elastic modulus using load and displacement sensing indentation experiments". *J. Mater. Res.*, 1992. **7**, p 1564.
- (17) A.G. Evans, Z. Suo, R. Z. Wang, I. A. Aksay, M. Y. He, J. W. Hutchinson, "Model for the Robust Mechanical Behavior of Nacre", *J. Mater. Res.* **16** [9] 2475-84 (2001).
- (18) R. Menig, M.H. Meyers, M.A. Meyers and K.S. Vecchio, "Quasi-static and dynamic mechanical response of *Haliotis Rufescens* (abalone) shells", *Acta materialia*, **48** (2000), 2383-2398.
- (19) F. Barthelet, and H.D. Espinosa, "Elastic Properties of Nacre Aragonite Tablets", *Proceedings of the 2003 SEM Annual Conference and Exposition on Experimental and Applied Mechanics*, June 2-4, Charlotte, North Carolina, Session 68, Paper 187, 2003.
- (20) X. Li and P. Nardi, "Micro/nanomechanical characterization of a natural nano-composite material - the shell of Pectinidae", *Nanotechnology* **15** (2004) 211-217
- (21) Van Vliet, K.J., et al., "Quantifying the early stage of plasticity through nanoscale experiments and simulations." *Physical Review*, 2003. **B67**: p. 104105.
- (22) Matthew Jurgens, "Atomic Structure of Aragonite"
<http://www.und.edu/instruct/mineral/geol318/webpage/jurgens/>
- (23) Monica Fritz, "Research Website,"
<http://www.biophysik.uni-bremen.de/fritz/research.html>